remote sensing

MDPI

Article

Pragmatically Mapping *Phragmites* with Unoccupied Aerial Systems: A Comparison of Invasive Species Land Cover Classification Using RGB and Multispectral Imagery

Alexandra Danielle Evans [1,*], Jennifer Cramer [1], Victoria Scholl [2] and Erika Lentz [1]

[1] United States Geological Survey, Woods Hole Coastal and Marine Science Center, Woods Hole, MA 02543, USA; jcramer@usgs.gov (J.C.); elentz@usgs.gov (E.L.)
[2] United States Geological Survey, Geosciences and Environmental Change Science Center, Denver, CO 80225, USA; vscholl@usgs.gov
* Correspondence: adevans@usgs.gov

Abstract: Unoccupied aerial systems (UASs) are increasingly being deployed in coastal environments to rapidly map and monitor changes to geomorphology, vegetation, and infrastructure, particularly in difficult to access areas. UAS data, relative to airplane or satellite data, typically have higher spatial resolution, sensor customization, and increased flexibility in temporal resolution, which benefits monitoring applications. UAS data have been used to map and monitor invasive species occurrence and expansion, such as *Phragmites australis*, a reed species in wetlands throughout the eastern United States. To date, the work on this species has been largely opportunistic or ad hoc. Here, we statistically and qualitatively compare results from several sensors and classification workflows to develop baseline understanding of the accuracy of different approaches used to map *Phragmites*. Two types of UAS imagery were collected in a *Phragmites*-invaded salt marsh setting—natural color red-green-blue (RGB) imagery and multispectral imagery spanning visible and near infrared wavelengths. We evaluated whether one imagery type provided significantly better classification results for mapping land cover than the other, also considering trade-offs like overall accuracy, financial costs, and effort. We tested the transferability of classification workflows that provided the highest thematic accuracy to another barrier island environment with known *Phragmites* stands. We showed that both UAS sensor types were effective in classifying *Phragmites* cover, with neither resulting in significantly better classification results than the other for *Phragmites* detection (overall accuracy up to 0.95, *Phragmites* recall up to 0.86 at the pilot study site). We also found the highest accuracy workflows were transferrable to sites in a barrier island setting, although the quality of results varied across these sites (overall accuracy up to 0.97, *Phragmites* recall up to 0.90 at the additional study sites).

Keywords: structure-from-motion; feature importance; aerial imagery; method comparison; image classification; machine learning

check for updates

Citation: Evans, A.D.; Cramer, J.; Scholl, V.; Lentz, E. Pragmatically Mapping *Phragmites* with Unoccupied Aerial Systems: A Comparison of Invasive Species Land Cover Classification Using RGB and Multispectral Imagery. *Remote Sens.* **2024**, *16*, 4691. https://doi.org/10.3390/rs16244691

Academic Editor: John Dymond

Received: 1 November 2024
Revised: 5 December 2024
Accepted: 9 December 2024
Published: 16 December 2024

Copyright: © 2024 by the authors. Licensee MDPI, Basel, Switzerland. This article is an open access article distributed under the terms and conditions of the Creative Commons Attribution (CC BY) license (https://creativecommons.org/licenses/by/4.0/).

1. Introduction

Unoccupied aerial systems (UASs), also known as drones [1], are increasingly being deployed in coastal environments to rapidly map and monitor changes to geomorphology, vegetation, and infrastructure, particularly in difficult to access areas. UAS data, relative to airplane or satellite data, have benefits of higher spatial resolution, sensor customization, and flexibility in temporal resolution [2]. UAS imagery can be particularly useful for identifying invasive vegetation, which can be difficult to survey from the ground due to challenges in navigating natural environments [3]. The map scale and classification accuracy provided by UAS data makes it suitable for ecological applications, including invasive species management [4–11].

Here, we evaluate the use of UASs for detecting invasive species, with *Phragmites australis* (hereafter "*Phragmites*") as an example. *Phragmites* is an opportunistic reed species expanding in wetland environments throughout the eastern United States [12,13]. *Phragmites* expansion is linked to site disturbance and development [12,14–16] and may continue in coastal ecosystems due to rising sea levels [17]. *Phragmites* poses ecological threats [12], including the reduction of habitat quality for some species [18–21]. However, *Phragmites* stands can provide protective buffering from storms [22] and increase sediment accretion rates [23], which can be important services in coastal areas facing sea-level rise and increased storm activity.

The remote sensing community has a history of exploring methods to detect *Phragmites*, with studies dating back to the 1980s using satellite and airborne (e.g., plane) imagery and other data (e.g., [4,15,24–40]). Remote sensing has also been used to evaluate changes in invasive species' health [41,42]. However, plane imagery can be expensive to acquire, satellite imagery is provided at relatively coarse resolutions, and both sources have limitations regarding how fine a temporal resolution can be acquired due to costs or satellite return intervals. Therefore, plane and satellite imagery can be limited options for pre-/post-restoration monitoring and adaptive management. There is a lack of post-treatment monitoring in *Phragmites* management projects, partially due to financial and logistical constraints [12]. Communities must weigh the ecosystem services provided by *Phragmites* against its ecological threats when making management decisions, and these decisions are case-specific [12,43], requiring higher resolution information that can be provided by UASs.

UASs have been used to monitor invasive species such as *Phragmites* with various sensors and classification workflows (e.g., [3–5,8,11,44–48]). Ref. [11] achieved 94.80% overall accuracy using a pixel-based neural network with multispectral imagery and a canopy height model to map *Phragmites* and other vegetation species. Ref. [8] found object-based classification methods with red-green-blue (RGB) imagery worked well for mapping dead *Phragmites*, live *Phragmites*, other vegetation, and not vegetation, with overall classification accuracy >90%. Ref. [45] used multispectral imagery in a multiclass relevance vector machine to map *Phragmites*, other mixed vegetation, salt, muddy water, and water, producing overall accuracies of 90% and greater. Ref. [49] used RGB imagery in convolutional neural networks to estimate *Phragmites*, leaf litter, water, bare ground, and other vegetation cover and found their methods estimated *Phragmites* at accuracies >98%. With these varied efforts, a baseline understanding of the differences in costs and efficacy is key for their feasibility in site monitoring.

In this paper, we propose a general methodology comparison that considers the tradeoffs of common sensors in wetlands mapping (red-green-blue (RGB) and multispectral sensors) [5]. We statistically and qualitatively compare the classification results from digital surface models (DSMs, models of vegetation canopy elevation) and image orthomosaics from two types of UAS data: (1) RGB imagery collected with a Ricoh GRII camera (Ricoh Imaging Company, Ltd., Tokyo, Japan) and (2) multispectral imagery collected with either a MicaSense RedEdge-3 or a MicaSense Altum-PT multi-lens sensor (AgEagle Aerial Systems Inc., Wichita, KS, USA), both processed using structure-from-motion (SfM) photogrammetry software (Agisoft Metashape Professional edition 1.7.5 for the pilot site and edition 1.8.x for the additional sites (Agisoft LLC., St. Petersburg, Russia)). Although canopy height models, which can be created from DSMs and digital elevation models (DEMs; topographic models of bare earth), can improve classification capabilities, they can be challenging to acquire via SfM in densely vegetated and inundated environments. Water presence leads to refraction effects in elevation values [50], and dense vegetation cannot be properly filtered to create an accurate DEM as there is an insufficient amount of bare ground visible in the model to reliably interpolate [51,52]. This work addresses methodology research gaps regarding invasive species cover classification that take full advantage of the spectral and topographic information acquired via SfM.

It is important to understand the efficacy and trade-offs of the RGB and multispectral orthomosaics and DSMs as used in image classification workflows. Previous studies have

taken advantage of more sophisticated topographic information like canopy height models or have solely used one sensor or the other rather than compare RGB vs. multispectral results. Determining how spectral and topographic information from one sensor compares relative to including more sophisticated sensors in invasive species monitoring methods can help users determine optimal study design given resources and capacity. We use pixel-based classification approaches, which have out-performed object-based approaches in wetland environments [11,53]. We examine the hypothesis that multispectral imagery can provide significantly better land cover classification results than RGB imagery, and that workflows that provided high thematic accuracy would be transferable to other study sites.

Deep learning methods are powerful tools for image classification and segmentation and are being tested in the remote sensing field for mapping invasive species (e.g., [49]). *Phragmites* has a strong correlation with the surrounding environment (e.g., adjacent to other *Phragmites* individuals in stands). Therefore, approaches like convolutional neural networks or transformer-based networks that can effectively utilize image contextual information could be apt tools for identifying *Phragmites*, as demonstrated by [49] and suggested as possible by the findings of studies such as [54–56].

The work herein uses the random forest algorithm rather than deep learning approaches for the following reasons. First, more traditional machine learning algorithms, such as random forest, are currently widely available in both code libraries as well as boxed GIS workflows that take advantage of graphical user interfaces for accessibility. There is increasing availability of deep learning tools in such software, but until these methods are more widely known and accessible, we opted to test a more conventional classification approach. Second, deep learning approaches require large datasets to train and test. Transfer learning [57] can be taken advantage of depending on the type of imagery being used, but the amount of data needed to effectively test both the RGB and multispectral sensors across the sites was a significant obstacle in the potential study design. Until labeled data repositories useful for training and testing UAS-based land cover classification algorithms are available, labeling train and test data can be a significant and resource intensive task. A rapid human-in-the-loop segmentation approach [58] is one potential way of generating such labeled data to support future studies. Such approaches can be incorporated into and tested in future work. Third, deep learning requires relatively more computational power than simpler image classification approaches. These required resources can also limit accessibility to the methods for others interested in using them. In general, our study design was mindful of the current capacity accessibility of the methods as seen from an ecological practitioner or land manager perspective and strove for the findings to be relevant for such parties' decision-making, while acknowledging that deep learning approaches are worth exploring in future method comparison work as they become more commonplace.

2. Materials and Methods

Our study design evaluated both sensor types as well as the transferability of classification workflows. We first conducted a pilot study on Cape Cod, Massachusetts, USA, to establish data processing and classification workflows, and then used these results to evaluate the transferability of our methods to a barrier island site in Maryland, USA (Figure 1).

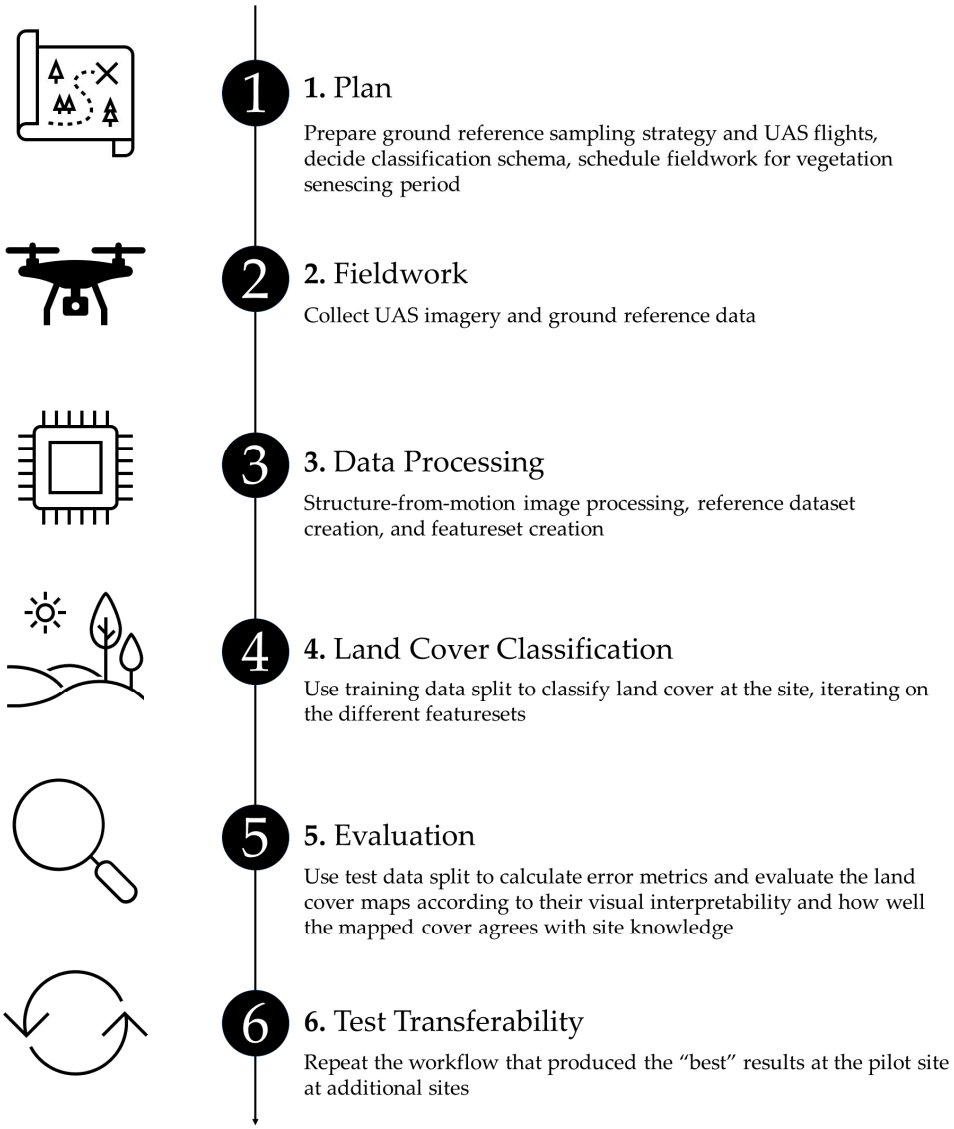

Figure 1. Flowchart illustrating the overall study design.

2.1. Pilot Study: Dog Head Marsh Setting and Data Collection

A salt marsh within the Waquoit Bay National Estuarine Research Reserve (referred to as "Dog Head Marsh", or DHM hereafter) in Cape Cod, MA, USA, served as our pilot site (Figure 2). The marsh has a main channel surrounded primarily by low-elevation marsh vegetation, dominated by *Spartina alterniflora* and *Patens*, *Distichlis*, and *Scirpus*. *Salicornia* was also present in patches. *Phragmites* was abundant along the marsh edges. We conducted fieldwork [59] late in the growing season when the spectral signature of senescing *Phragmites* can be more easily distinguished from that of surrounding vegetation [33]. Imagery was collected and locations were measured at ten ground control points (GCP) on 7 October 2021 (Supplementary Materials S1).

UAS flights were completed during a 4 h window +/− 2 h around solar noon (1230 EDT). RGB imagery was collected with a Ricoh GRII camera (Ricoh Imaging Company, Ltd., Tokyo, Japan), and multispectral imagery was collected with a MicaSense RedEdge-3 multi-lens sensor (AgEagle Aerial Systems Inc., Wichita, KS, USA). The two sensors were flown separately on a 3DR Solo UAS (3D Robotics, Inc., Berkeley, CA, USA). For the RGB sensor, automated flight paths were designed to be flown at 100 m above ground level with 70% side overlap planned across the images. The camera's intervalometer was set to shoot every 2 s and the UAS was set to fly at a speed of 7 m per second along the flight lines,

obtaining sufficient forward image overlap for SfM. The RGB flights were completed from 11:15 a.m. EDT to 11:45 a.m. EDT. For the multispectral sensor, automated flight paths were designed to be flown at 80 m above ground level with 70% side overlap planned across the images. The camera was set to overlap mode at 75% and the UAS was set to fly at a speed of 5 m per second along the flight lines, obtaining sufficient image overlap for SfM. The multispectral flights were completed from 12:04 p.m. EDT to 12:51 p.m. EDT. See Supplementary Materials S2 for additional details on the UAS flights, such as weather conditions.

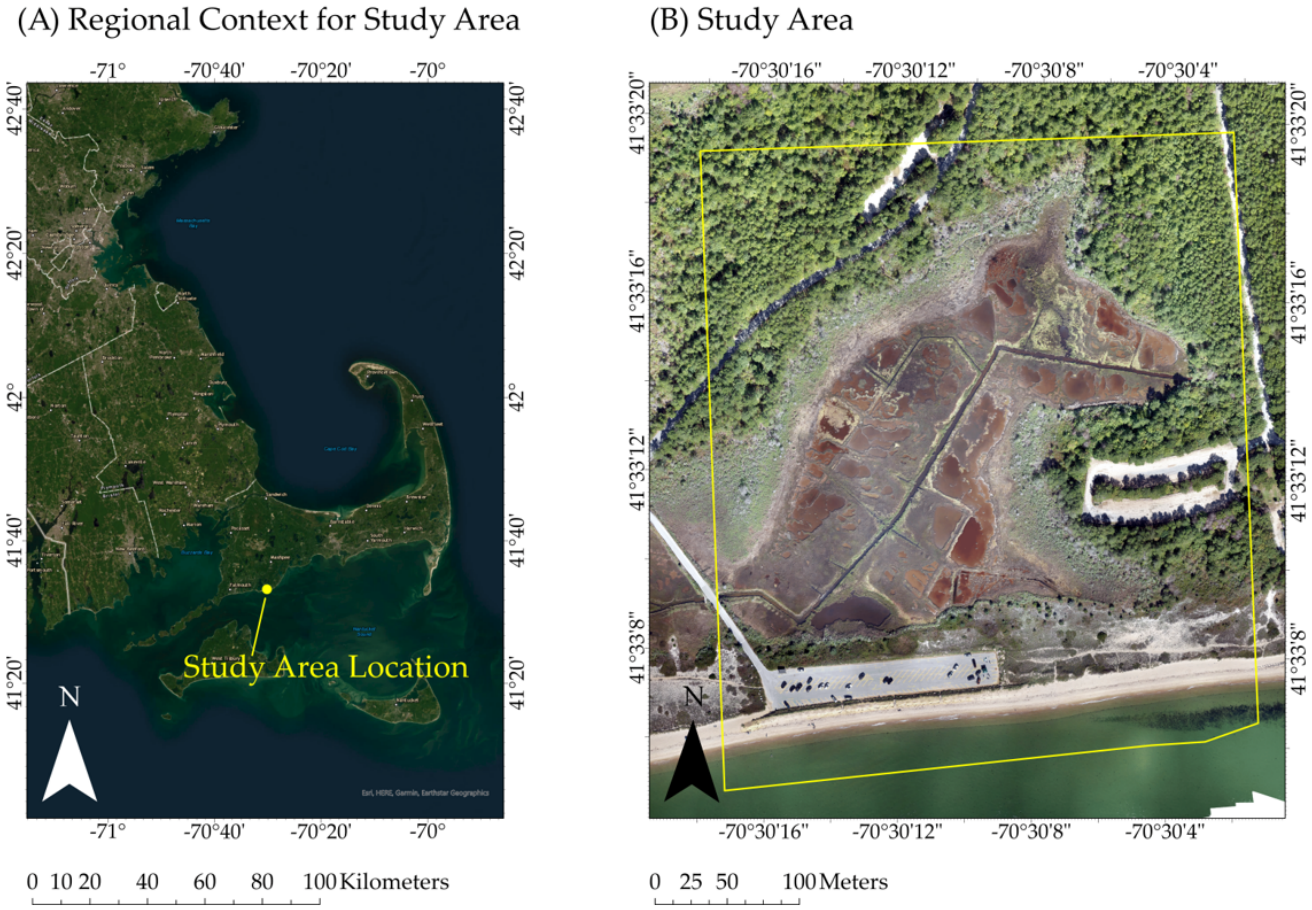

Figure 2. (**A**) Regional map of Cape Cod showing the location of Dog Head Marsh in Mashpee, MA, USA. (**B**) Study site orthomosaic from the uncrewed aerial system RGB sensor. The yellow box in (**B**) indicates the study area.

We measured elevation and land cover at 169 unmarked validation points (data points throughout the site that were not physically marked in the landscape like ground control points) on 8 October, the day after image collection. These points served as base reference data for the *Phragmites* classification workflows and the vertical accuracy of the DSMs. We classified the land cover at each point as (1) "*Phragmites*", (2) "other vegetation", and (3) "not vegetation". Although exact locations of these unmarked validation points were unplanned, care was taken to collect a minimum of ten measurements per land cover class and to distribute these points across the site without clustering. At each point, vegetation species and other cover within a 6 inch (15.24 cm) radius from the survey rod tip were estimated. Vegetation height was noted by measuring the height of the plant individual closest to the survey rod. We took photographs of each measurement location for later reference. We accepted points with at least 50% *Phragmites* cover as *Phragmites* reference data (22 points). All other points collected in vegetated terrain were assigned to the "other vegetation" class (96 points), and 51 points were collected in "not vegetation" cover. The X, Y, and Z locations

of these points were measured using a Spectra Precision (SP80) Global Navigation Satellite System (GNSS) Receiver (Trimble Inc., Westminster, CO, USA) in real-time kinematic mode using corrections from the Massachusetts continuously operated reference station (CORS) network. Measurements at local benchmarks and previous experience with this equipment indicate that our survey accuracy was within the instrument specifications of 1.57 cm for horizontal (XY) and 2.94 cm for vertical (Z) positioning.

2.2. Pilot Study: Structure-from-Motion Photogrammetry

DSMs and orthomosaics for DHM were created via SfM using Agisoft Metashape Professional edition 1.7.5 (Agisoft LLC., St. Petersburg, Russia). Our workflows were adapted from [60] and the Agisoft and MicaSense documentation [61]. We adapted the [60] workflow for our goal of classifying vegetation, rather than for optimizing topographic accuracy in unvegetated areas. For example, we used a milder point filter setting to preserve the reconstruction of vegetated surfaces [62]. GCP accuracy metrics were provided by Metashape. See Supplementary Materials S3 for details on the SfM workflow.

2.3. Pilot Study: Reference Dataset Creation

We extended our reference data by labeling additional points using a multinomial sampling model (Supplementary Materials S4, Equation (S3)) [63] to enable the calculation of statistically valid error matrices. Our calculations indicate that 482 reference points were needed to fill the error matrix (details in Supplementary Materials S4). We proportionately distributed the additional points across the three land cover classes based on their approximated cover while maintaining a minimum of 50 samples for the rarest cover class, which was *Phragmites* [63]. To add reference data, we visually interpreted the orthomosaic guided by the unmarked validation points, and manually added points in our geographic information system (GIS). We added enough points to double the amount of reference data so we could use a 50%/50% train/test split for each class. After doubling, we had a final set of 100 *Phragmites* samples (50 per split), 674 "other vegetation" samples (337 per split), and 190 "not vegetation" samples (95 per split).

2.4. Pilot Study: Featureset Creation

Features were extracted from the SfM products (Table 1) that captured different types of information from the orthomosaic and DSM rasters: band spectral values, reflectance, and topography. Features included original bands from the raster products (3 or 5 bands from the orthomosaic and one band from the DSM), a vegetation index, eight Haralick texture features [64–66], and DSM rugosity.

Haralick texture features are commonly used in image analysis to describe image texture and are based on grayscale spatial dependencies calculated from imagery [64,67]. DSM rugosity, a texture metric from the DSM, was calculated as the standard deviation of a pixel neighborhood (8 surrounding pixels) in a moving window [53]. DSM rugosity captures local variation in vegetation structure and can thus aid classification [53], particularly for *Phragmites*, whose tall reed structure may result in higher rugosity values.

The Green Leaf Index (GLI) is a visible vegetation index where negative values tend to be soil/non-living cover while positive values are green leaves and stems (Supplementary Materials S4, Equation (S4)) [68]. We used the GLI over other visible-spectrum vegetation indices (e.g., Visible Atmospherically Resistant Index, Vegetation Index Green) [69] as GLI has been shown to be more effective in detecting differences between vegetation and non-vegetation in imagery [70]. The Normalized Difference Vegetation Index (NDVI) is a widely used vegetation index (Supplementary Materials S4, Equation (S5)) [71,72] that takes advantage of the near-infrared bands provided by the multispectral sensor.

Table 1. The spectral-based and structure-based bands ("features") generated from the raster products for the classification analysis. Each feature is considered either spectral or structural, as indicated per row in the "Spectral Metric" or "Structural Metric" columns. "RGB" refers to the RGB sensor data while "Multi" refers to the multispectral sensor data. The spatial resolutions of the structural metrics are 3 cm for the RGB data and 5 cm for the multispectral data. The documentation of textures (description and formulas) is available in the OTB CookBook section 'Textures' [66].

Feature Name	Spectral Metric RGB (3 cm Resolution)	Spectral Metric Multi (5 cm Resolution)	Structural Metric
Red	Digital Number (0 to 255)	Reflectance (0 to 1)	
Green	Digital Number (0 to 255)	Reflectance (0 to 1)	
Blue	Digital Number (0 to 255)	Reflectance (0 to 1)	
Red Edge	NA	Reflectance (0 to 1)	
Near-infrared (NIR)	NA	Reflectance (0 to 1)	
Green Leaf Index	Index between –1 and 1	NA	
Normalized Difference Vegetation Index	NA	Index between –1 and 1	
Local Haralick Textures (Calculated from a grayscale version of the RGB orthomosaic or the NIR band from the multispectral orthomosaic using 8 neighbor pixels in Orfeo Toolbox)	Energy		
	Entropy		
	Correlation		
	Inverse Difference Moment (IDM)		
	Inertia		
	Cluster Shade		
	Cluster Prominence		
	Haralick Correlation		
Digital Surface Model (DSM)			Surface Height (m)
DSM Rugosity			SD of Surface Height (m) of 8 neighbor pixels

We sought a model that would be successful in pixel-based classification of raster data. To do so, we tested combinations of raster products ("features"), called "featuresets", that serve as input into models to determine which were more successful in discriminating among the land cover classes and identifying *Phragmites*. Table 2 describes the "featuresets" tested in the classification workflow. Featuresets were designed based on the two types of raster products: DSMs and orthomosaics. "All Features" included all features obtained from both products from each sensor (Table 2). However, supplying correlated, and, thus, redundant, features to a classifier such as a random forest can lead to decreased model accuracy [73]. We used Spearman's rank coefficient [74] to identify features that were well correlated (absolute $\rho > 0.8$), and constructed featuresets that included only uncorrelated features. For example, in one RGB classification scenario, we found that "entropy" and "cluster prominence" were highly correlated ($\rho = 0.87$) but that "energy" and "red" were not well correlated ($\rho = -0.10$), indicating they contributed independent information to the model. In other iterations, we used features solely from the DSM or orthomosaic to see how well classifications would perform (1) without DSM topography information ("All Features from Orthomosaic") and (2) solely with DSM information ("Features from DSM"). Please see the rendered notebook html files in the Supporting Information for full details of the code used to create the featuresets.

Table 2. Featuresets used in the classification workflow comparison. A gray box with an "x" indicates that a feature is included in a featureset. The feature names correspond to their definitions in Table 1. For example, the "Blue" feature for the RGB sensor is a digital number, while the "Blue" feature for the multispectral is reflectance. Feature names are as initially given in Table 1 except "R" is red, "G" is green, "B" is blue, "R.E." is red edge, "Ener." is energy, "Entr." is entropy, "Corr." is correlation, "Inert." is inertia, "C.S." is cluster shadow, "C.P." is cluster prominence, "H.C." is Haralick correlation, and "D.R." is DSM rugosity.

Sensor	Featureset	Included Features																
		R	**G**	**B**	**R.E.**	**NIR**	**GLI**	**NDVI**	**Ener.**	**Entr.**	**Corr.**	**IDM**	**Inert.**	**C.S.**	**C.P.**	**H.C.**	**DSM**	**D.R.**
RGB	All Features	x	x	x			x		x	x	x	x	x	x	x	x	x	x
	All Uncorrelated Features	x					x		x		x			x			x	x
	All Features from Orthomosaic	x	x	x			x		x	x	x	x	x	x	x	x		
	Uncorrelated Features from Orthomosaic	x					x		x		x			x				
	Features from DSM																x	x
Multispectral	All Features	x	x	x	x	x		x	x	x	x	x	x	x	x	x	x	x
	All Uncorrelated Features			x				x	x		x			x		x	x	x
	All Features from Orthomosaic	x	x	x	x	x		x	x	x	x	x	x	x	x	x		
	Uncorrelated Features from Orthomosaic			x				x	x		x			x		x		
	Features from DSM																x	x

2.5. Pilot Study: Land Cover Classification

Feature importance metrics are useful when considering which features to prioritize in data collection and analysis. We used the random forest (RF) algorithm because it is commonly available in both code libraries and GIS software and enables exploration of feature importance [75]. An RF algorithm was trained for and applied to each featureset in Table 2 using the scikit-learn library (version 1.0.1) [76]. The same points in the 50% train split containing the extracted feature values for each featureset were used for training the algorithm for each scenario. Each RF was tuned to its respective featureset training data by using random search (to narrow the hyperparameter range; RandomizedSearchCV in scikit-learn) with five stratified K-fold splits for cross validation; then, grid search (GridSearchCV in scikit-learn) was used to further limit the hyperparameter range, with the resulting best parameters then used to fit each RF model. The fitted RF was applied to the entire respective featureset raster representing the site, resulting in a classified cover map. Please see the rendered notebook html files in the Supporting Information for full details of the code used to complete the classification workflow.

2.6. Pilot Study: Evaluation

Feature importance metrics (mean decrease in impurity and permutation on the full model from scikit learn), error matrices, and accuracy metrics were generated post-model fitting with the test data split. The same test point locations were used across the classification results. Our accuracy metrics included precision, recall, F1-score, user's and producer's accuracy per class, along with overall accuracy and the Kappa statistic (KHAT). Recall is important when the cost of a false negative is high (e.g., not classifying *Phragmites* cover where there is some) and tells us how well true positives were identified (a.k.a. the "true positive rate"). Given an error matrix, recall is calculated by dividing the number of true positives by the sum of the number of true positives and false negatives and gives values from 0 to 1, where values closer to 1 indicate more reliable results. *Phragmites* recall was particularly important in our consideration of "best performing" workflows, as the cost of a false negative in invasive species management can result in further spread and ineffective management.

KHAT has limitations as an accuracy metric on its own [77], but it can be used to compare two error matrices and determine if one is statistically significantly different than another. We used this approach to determine if the "best performing" featureset from each sensor provided statistically significantly different classification results by comparing KHAT values via the Z statistic following [63] (pp. 127–132) (detailed in Supplementary Materials S5). Please see the rendered notebook html files in the Supporting Information for full details of the code used to complete the different evaluations, including accuracy metrics and Z statistic calculations.

2.7. Applying the "Best" Methods from the Pilot Study to New Sites

We applied the "best" classification workflow per sensor from the DHM pilot site to five *Phragmites*-invaded sites at Assateague National Seashore, Maryland, USA (hereafter "ASIS"; Figure 3). Fieldwork at ASIS was completed 10–14 October 2022 [78], during the *Phragmites* senescing period. We also tested an "uncorrelated" featureset to determine if the "best" featureset provided correlated features. The "best" workflows from the DHM were determined by considering (1) the accuracy metrics, with emphasis placed on *Phragmites* recall, (2) the visual interpretability of the results, and (3) if mapped locations of *Phragmites* agreed with our site knowledge.

ASIS fieldwork, processing, and analysis were like the DHM but differed as we improved our methods and upgraded equipment. See Supplementary Materials S6 for details on the differences between the DHM and the ASIS sites fieldwork and processing. For example, we used a MicaSense Altum-PT (AgEagle Aerial Systems Inc., Wichita, KS, USA) multispectral sensor with higher spatial resolution for each band rather than the MicaSense RedEdge-3. We prepared 50 randomly generated points per site in GIS prior to

fieldwork to improve the sampling of our unmarked validation points. See Supplementary Materials S7 for reference data distributions across the classes for each ASIS site. We used the KHAT-based approach (outlined in Supplementary Materials S5) to compare two error matrices, one from RGB data and one from multispectral data, produced per the "best" site and the "worst" site's classified results.

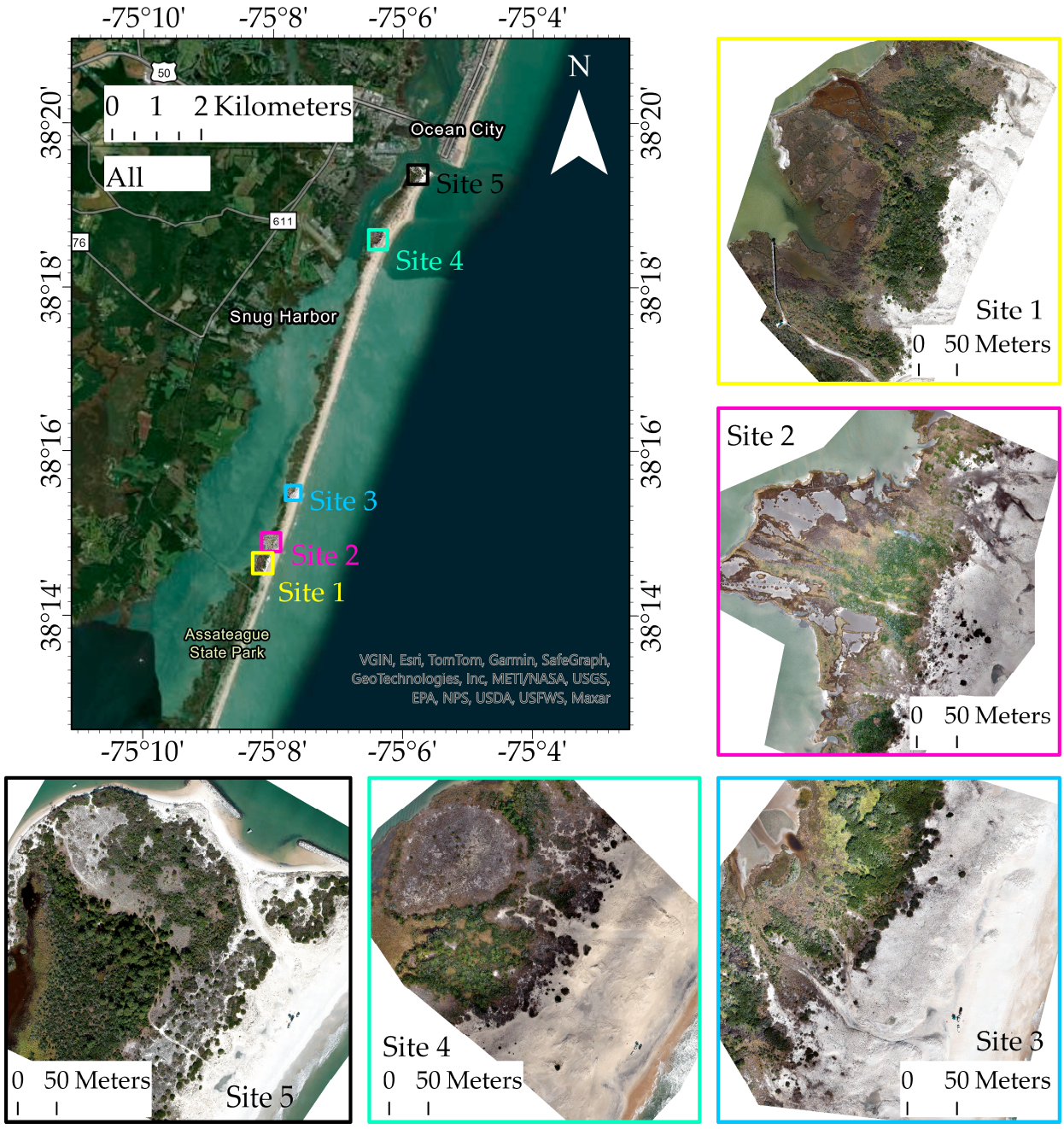

Figure 3. Locations of the five study sites in the northern section of Assateague National Seashore (Maryland, USA). Zoomed-in views of clipped orthomosaics made from the RGB imagery are labeled and shown to the right and bottom of the "All Sites" panel.

We also explored the effects of smoothing the ASIS classification results with majority filters. Majority filters have been used on pixel-based classified images to reduce their "salt-and-pepper" effect [79]. We hypothesized applying majority filters would improve the visual interpretability of classified cover maps but also impact their accuracy metrics. We used the SciPy library (version 1.7.3) [80] to apply both size 3 and size 5 majority filters

(written using the "generic_filter" function, see Supplementary Materials for details) to the "best" and "worst" sites' classified results. The "best" and "worst" site results were determined by considering the same three aspects considered when determining the DHM site's "best" workflows, i.e., (1) accuracy, (2) visual interpretability, and (3) agreement with our site knowledge. We recalculated error metrics for the smoothed classified results using the same test points as the unsmoothed results. Please see the rendered notebook html files in the Supporting Information for full details of the code used to complete the ASIS featureset creation, classification workflow, and evaluations.

3. Results

3.1. UAS Product Quality for Visual Interpretation

The orthomosaics produced for all sites were of sufficient quality to visually identify *Phragmites* (Figure 4). *Phragmites* stand size, shape, and individuals separated from stands can be observed in the imagery by careful observation. These observations can be used to create training and/or test data for models, create maps of cover via manual digitization, and provide visual observations of *Phragmites* conditions at a site. *Phragmites* exhibits distinctive leaf shape and structure (individual plants look like stars) and plumes that can distinguish it from other vegetation. *Baccharis halimifolia* (a.k.a. "Groundsel"), which can appear similar, can be distinguished from *Phragmites* because its brighter white blooms are tightly clustered together relative to the individual *Phragmites* plumes. *Phragmites* stands appear in the DSM as bumpy-looking areas of relatively taller vegetation (Figure 4). However, mixed in and surrounding shrub cover can present a similar pattern in the DSM, so the spectral information from the orthomosaic is useful for discerning *Phragmites* stands from vegetation of similar heights.

3.2. Results from the Dog Head Marsh Pilot Study

Orthomosaics and DSMs produced for the DHM study site had sufficient spatial accuracy for the classification workflows (Table 3), as the GCP XY errors for the products were less than the pixel size of the products. Our vertical accuracy assessment revealed unvegetated terrain was more accurately modeled than vegetated terrain and the top of the canopy surface elevation tended to be underestimated (Supplementary Materials S8).

The tested featuresets provided results with high overall accuracy values (>0.8; Table 4). Featuresets that included information from both the orthomosaic and the DSM outperformed those that only contained information from either. The reliability of the results varied more when considering accuracy values specific to the *Phragmites* class. Considering *Phragmites*-specific metrics, the two "best" featuresets were "All Uncorrelated Features" for the RGB sensor and "All Features" for the multispectral sensor. Error matrices and accuracy metric reports for these featuresets can be found in Supplementary Materials S9 and S10. By comparing KHAT statistics (Supplementary Materials S5), we found the multispectral "All Features" classification results were not statistically significantly different than the RGB "All Uncorrelated Features" classification results. These two featureset types were applied to the ASIS data. The "All Features" RGB featureset and the "All Uncorrelated Features" multispectral featureset were close to the "best" performers, but the differences in metric values were minute, and we deemed them not worth intensively testing at additional sites. We did apply the "All Uncorrelated Features" multispectral featureset to a limited number of ASIS sites.

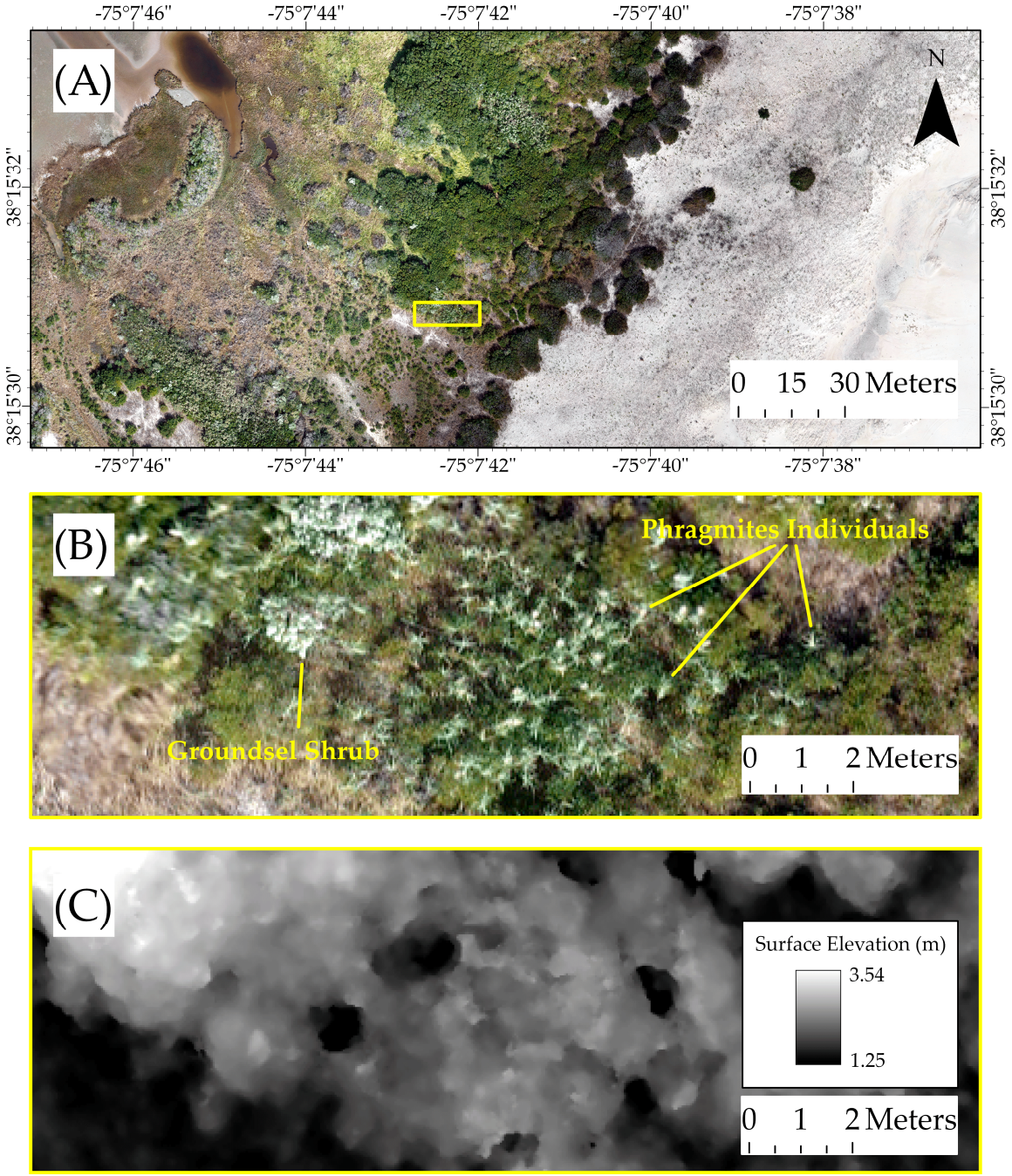

Figure 4. (**A**) A section of the RGB orthomosaic for ASIS Site 3. The yellow extent indicator corresponds to panel (**B**). (**B**) A zoomed-in view of the orthomosaic, illustrating how individual *Phragmites* plants, both with and without plumes, can be visually identified in the imagery. *Phragmites* can also be visually distinguished from similar looking species, such as *Baccharis halimifolia* (a.k.a. "Groundsel"). (**C**) The same geographic extent shown in (**B**) but showing the digital surface model rather than the RGB orthomosaic.

Feature importance metrics generated from the RFs trained on the "All Features" featuresets consistently identified the vegetation index and the DSM elevation features as some of the most important features for the classification (Figure 5). This further supports the importance of having information from both the orthomosaic and the DSM in a featureset.

Table 3. Positional accuracy metrics for the Dog Head Marsh uncrewed aerial system products based on the ground control point (GCP) information as generated by Agisoft Metashape Professional. The same set of GCPs (n = 10) were used to process both the RGB and multispectral imagery. The error estimates are provided by Agisoft Metashape as root mean square error values for the ground control positions.

Sensor	XY Error (cm)	Z Error (cm)	Total (cm)
RGB	0.8	1.9	2.1
Multispectral	0.7	0.7	1.0

Table 4. Bold rows indicate the featureset that produced the most reliable results per classification type per sensor according to the *Phragmites*-specific metrics (Precision, Recall, F1-score).

Sensor	Featureset	Precision *	Recall *	F1-Score *	Cohen Kappa	Overall Accuracy
RGB	All Features	0.87	0.68	0.76	0.82	0.92
	All Uncorrelated Features	**0.90**	**0.74**	**0.81**	**0.85**	**0.93**
	All Features from orthomosaic	0.55	0.22	0.31	0.56	0.82
	Uncorrelated Features from orthomosaic	0.38	0.18	0.24	0.53	0.81
	Features from DSM	0.66	0.58	0.62	0.73	0.88
Multispectral	**All Features**	**0.80**	**0.86**	**0.83**	**0.88**	**0.95**
	All Uncorrelated Features	0.79	0.84	0.82	0.87	0.94
	All Features from orthomosaic	0.58	0.30	0.39	0.72	0.88
	Uncorrelated Features from orthomosaic	0.53	0.32	0.40	0.70	0.87
	Features from DSM	0.60	0.62	0.61	0.62	0.83

* Values are specific to the *Phragmites* class.

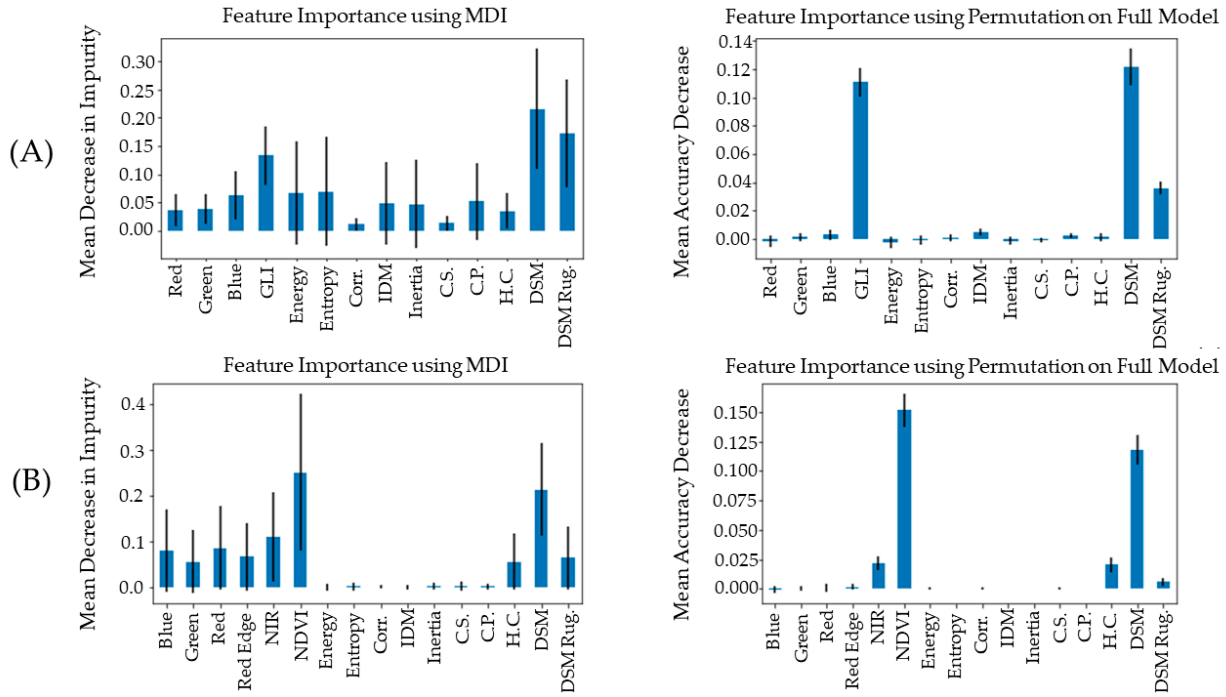

Figure 5. Feature importance metrics (mean decrease in impurity, "MDI", and permutation on full model) from the (**A**) RGB and (**B**) multispectral random forest classifications when using the "All Features" featuresets from Dog Head Marsh. Feature names are as initially given herein except "Corr." is correlation, "C.S." is cluster shadow, "C.P." is cluster prominence, "H.C." is Haralick correlation, and "DSM Rug." is DSM rugosity. The blue bars are the feature importances of the forest, along with their inter-tree variability represented by the error bars.

The "best" workflow from each sensor produced similar maps, labeling *Phragmites* around the edges of the marsh as "*Phragmites*" with some of the shorter dune vegetation mislabeled as "*Phragmites*" particularly in the multispectral results (Figure 6). Portions of the ocean in the RGB results were mislabeled as "Other Vegetation", where the multispectral correctly identified those regions as "Not Vegetation". The RGB results had a stronger visual "salt-and-pepper" effect. Differences in spectral and spatial resolution may have led to these discrepancies.

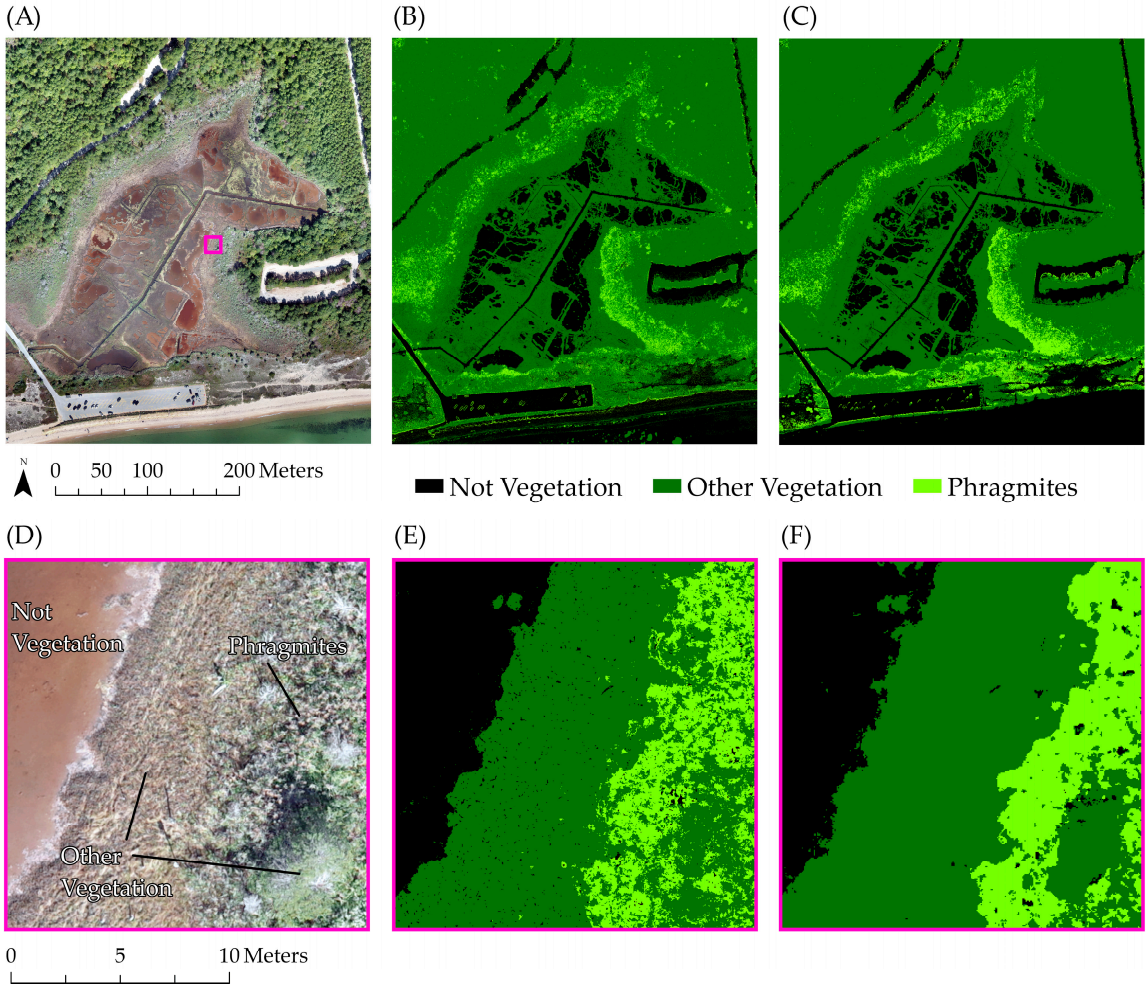

Figure 6. (**A**) The RGB orthomosaic for visual context. The "best" classified results (bold rows in Table 4) for the (**B**) RGB sensor and (**C**) multispectral sensor. (**D**) Zoomed-in view of an area containing *Phragmites*, other vegetation, and not vegetation, the extent of which is shown in (**A**) in pink. (**E**) The RGB classification of the area shown in (**D**). (**F**) The multispectral classification of the area shown in (**D**).

3.3. Results from the Sites at ASIS

Orthomosaics and DSMs produced for the ASIS sites had sufficient spatial accuracy for the classification workflows (Table 5). XY errors for the products were less than the pixel size of the products (4 cm for the Ricoh and 5 cm for the MicaSense).

Both sensors provided high overall accuracy values when the "best" featuresets ("All Uncorrelated Features" for the RGB, "All Features" for the multispectral) were used in the RF classification workflows (overall accuracy values > 0.9; Figure 7; Table of accuracy metrics in Supplementary Materials S11). The *Phragmites*-specific recall metric varied across the sites, with the RGB sensor generally producing higher *Phragmites*-specific metrics than

the multispectral sensor. ASIS accuracy metric reports and error matrices can be found in Supplementary Materials S12 and S13.

Table 5. Positional accuracy metrics for the uncrewed aerial system products based on the ground control point (GCP) information as generated by Agisoft Metashape. The error estimates are provided by Agisoft Metashape as root mean square error values for the ground control positions.

ASIS Site	Sensor	GCP Count **	XY Error (cm)	Z Error (cm)
1	RGB *	8	0.8	1.1
	Multispectral	10	1.6	2.5
2	RGB *	3	0.8	1.1
	Multispectral	3	1.2	0.05
3	RGB	11	1.3	1.9
	Multispectral	12	1.4	3.4
4	RGB	9	1.8	0.8
	Multispectral	10	2.0	2.3
5	RGB	9	1.2	1.6
	Multispectral	12	2.0	6.0

* For the RGB sensor, Site 1 and 2 were aligned together to help constrain the overlap and fewer GCPs of Site 2 and thus the errors are the same. ** The difference in GCP count is due to the use of check points in the RGB processing, some points were not used as control points.

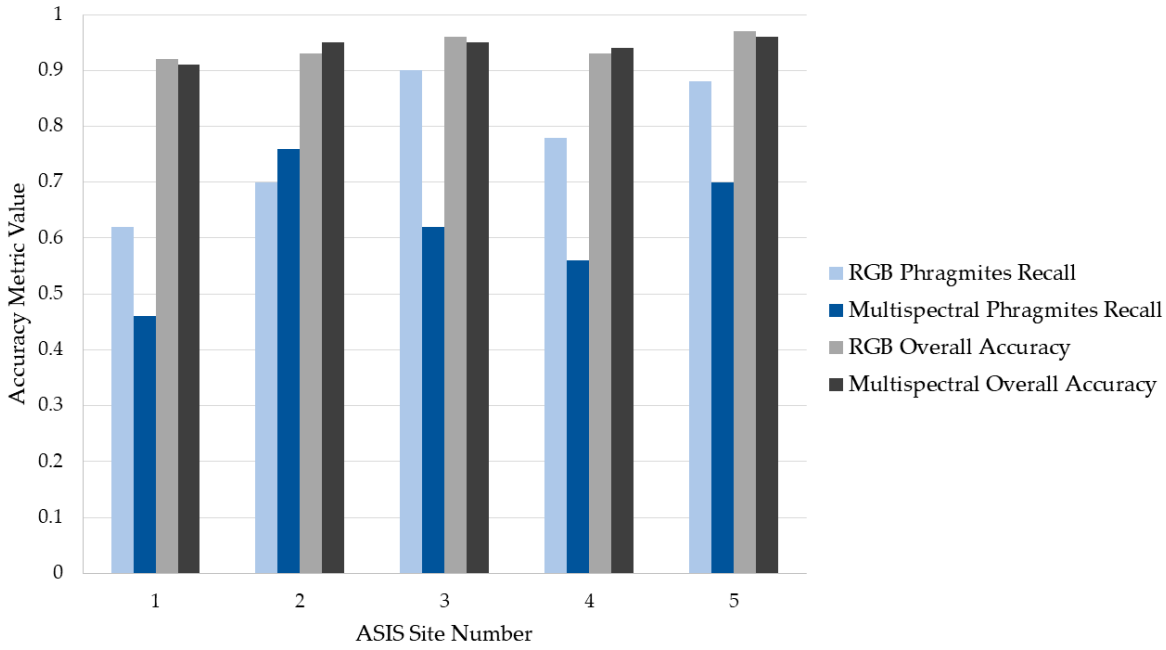

Figure 7. A comparison of select accuracy metrics calculated per sensor per Assateague (ASIS) site number. Recall is important when the cost of a false negative is high, as in invasive species management (e.g., not classifying *Phragmites* cover where there is some). Metric values closer to 1 indicate more reliable results.

Unlike the DHM, features identified as important by the RF were not as consistent across the ASIS workflows. Example important features from ASIS sites are shown in Figure 8. Example features are from the "best" and "worst" site results, ASIS 2 and 1, respectively, considering both the RGB and multispectral results. Unlike the DHM, the algorithms did not consistently identify the vegetation index and DSM feature as most important, but they were frequently identified as relatively important (Figure 8).

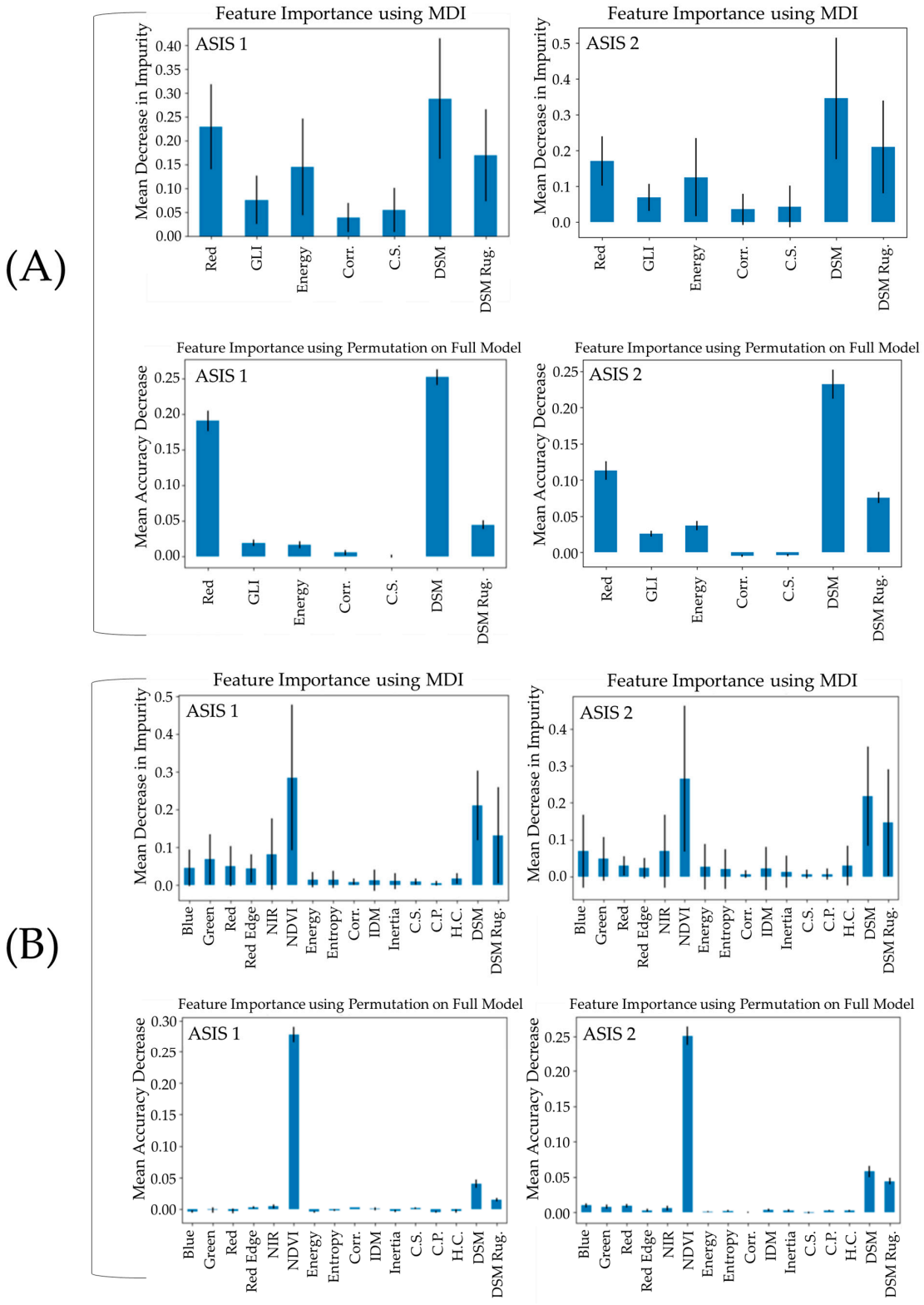

Figure 8. Bar plots showing example important features identified by the random forest algorithms trained and applied per Assateague (ASIS) site according to mean decrease in impurity and mean accuracy decrease metrics. These examples illustrate how the identified important features varied across sites and sensor types. The blue bars are the feature importances of the forest, along with their inter-tree variability represented by the error bars. Larger blue bars indicate higher importance. (**A**) RGB "All Uncorrelated Features" featureset. (**B**) Multispectral "All Features" featureset. Feature names are as initially given herein except "Corr." is correlation, "C.S." is cluster shadow, "C.P." is cluster prominence, "H.C." is Haralick correlation, and "DSM Rug." is DSM rugosity.

Classified maps for ASIS 2 and 1 are shown in Figure 9 (remaining maps in Supplementary Materials S14). Using the Kappa-based approach (outlined in Supplementary Materials S5), we statistically compared error matrices produced from the RGB and multispectral data at ASIS 1 and found them to be statistically similar. We repeated this approach for ASIS 2 and found them statistically similar. The relevant calculations for the ASIS sites can be found in Supplementary Materials S15.

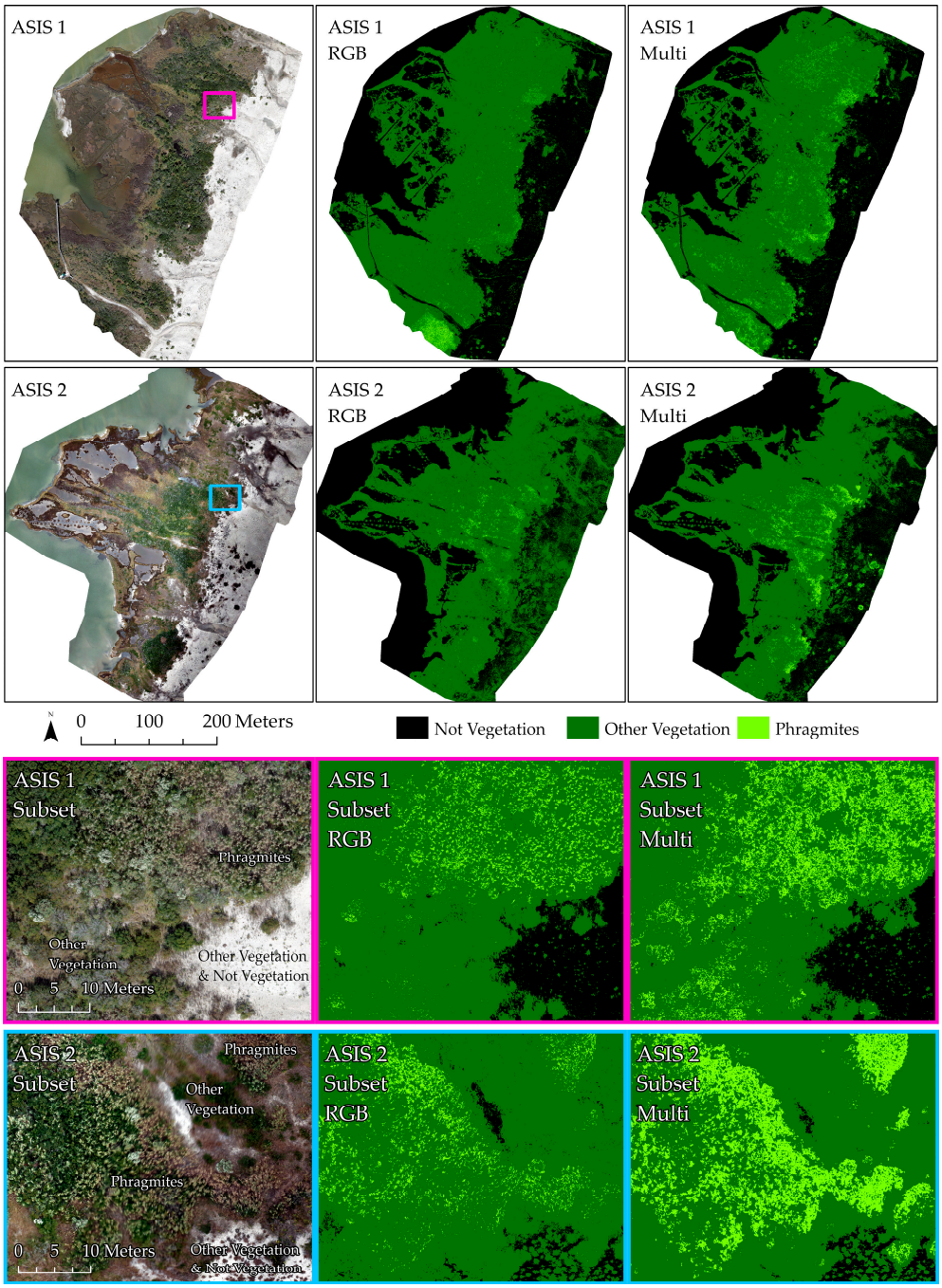

Figure 9. Classified cover maps for Assateague (ASIS) sites 1 and 2 from both the RGB and multispectral ("multi") data. The leftmost column is the RGB orthomosaic for each site, the middle column contains the RGB results, and the rightmost column is the multispectral results. The bottom two rows of panels show zoomed-in views of the sites along with their classified results. The extents of these subsets are shown in the "ASIS 1" and "ASIS 2" panels with pink and blue indicators, respectively.

We applied the "all uncorrelated features" multispectral workflow to ASIS 1 and 2 to check if the decreased performance of the "all features" workflow could be the result of supplying correlated features to the classifier [73]. At ASIS 2, the Spearman's rank coefficient identified the DSM feature as a correlated feature, so we did one workflow without it and one with it since the DSM feature was consistently identified as an important feature throughout this work. All tested workflows at ASIS 1 and 2 provided decreased performance relative to the DHM site according to the *Phragmites* recall metric (Table 6). Although the DSM feature was deemed correlated at ASIS 2, including it in the "All Uncorrelated Features + DSM Feature" featureset consistently improved the site results' accuracy metrics relative to the original "All Uncorrelated Features" featureset (Table 6).

Table 6. Accuracy metrics for multispectral results from the "best" and "second-best" workflows, identified per the Dog Head Marsh (DHM) pilot study, across select study sites.

Site	Featureset	Precision *	Recall *	F1-Score *	Cohen Kappa	Overall Accuracy
DHM	All Features	0.80	0.86	0.83	0.88	0.95
	All Uncorrelated Features	0.79	0.84	0.82	0.87	0.94
ASIS 1	All Features	0.61	0.46	0.52	0.83	0.91
	All Uncorrelated Features	0.58	0.56	0.57	0.82	0.90
ASIS 2	All Features	0.84	0.76	0.80	0.91	0.95
	All Uncorrelated Features **	0.76	0.62	0.68	0.87	0.93
	All Uncorrelated Features + DSM Feature	0.89	0.66	0.76	0.91	0.95

* *Phragmites* class-specific metric. ** Did not include the DSM feature since it was a correlated feature.

Figure 10 illustrates how smoothing can reduce the "salt-and-pepper" effect of the pixel-based classification, making it more visually interpretable by reducing noise around *Phragmites* stands. The shrub *Baccharis halimifolia* (a.k.a. "groundsel") tended to be mislabeled as "*Phragmites*" (Figure 10), likely due to the similar texture, heights, and color of the groundsel blooms. Bare branches in taller vegetation also tended to be mislabeled (Figure 10).

Smoothing influences the classification accuracies (Figure 11). *Phragmites* precision can improve with smoothing due to false positives being smoothed in classified results, with precision improving as the filter size increases. We found smoothing generally improves *Phragmites* precision based on the results from the "best" and "worst" ASIS sites' classified results from ASIS 2 and 1, respectively. Smoothing had less consistent impact on *Phragmites* recall at the two sites. *Phragmites* recall can be improved with smoothing due to erroneously labeled pixels located in denser *Phragmites* stands being properly labeled as "*Phragmites*" post-filtering. *Phragmites* recall can also decrease with smoothing due to properly labeled *Phragmites* pixels, sometimes representing freestanding individuals or sparser stands, being smoothed out. Overall accuracy remained consistent with smoothing (Supplementary Materials S16).

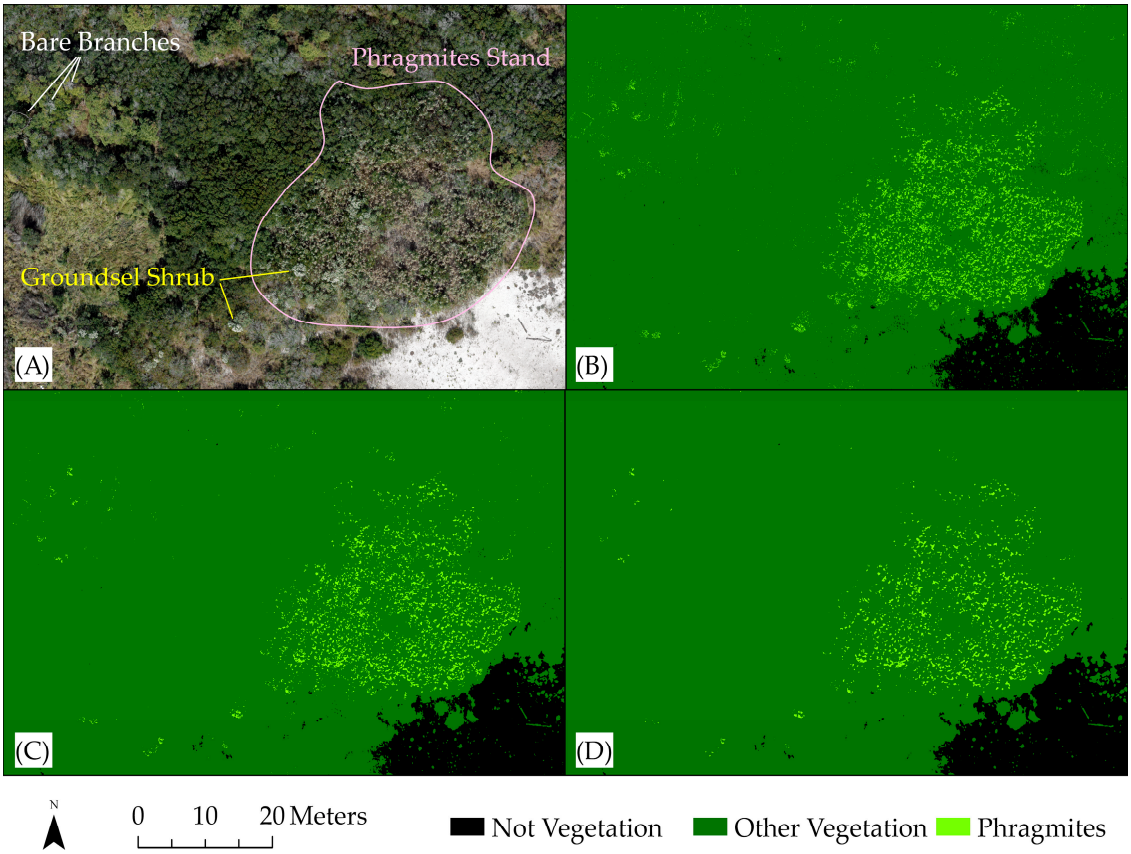

Figure 10. An example of how smoothing via majority filter impacts cover classification appearance. (**A**) The RGB orthomosaic for Assateague (ASIS) site 1 with the main *Phragmites* stand, example Groundsel shrubs, and example bare branches annotated. (**B**) The original classified results from the RGB data using the "All Uncorrelated Features" featureset. (**C**) The classified results from (**B**) smoothed with a size 3 majority filter. (**D**) The classified results from (**B**) smoothed with a size 5 majority filter.

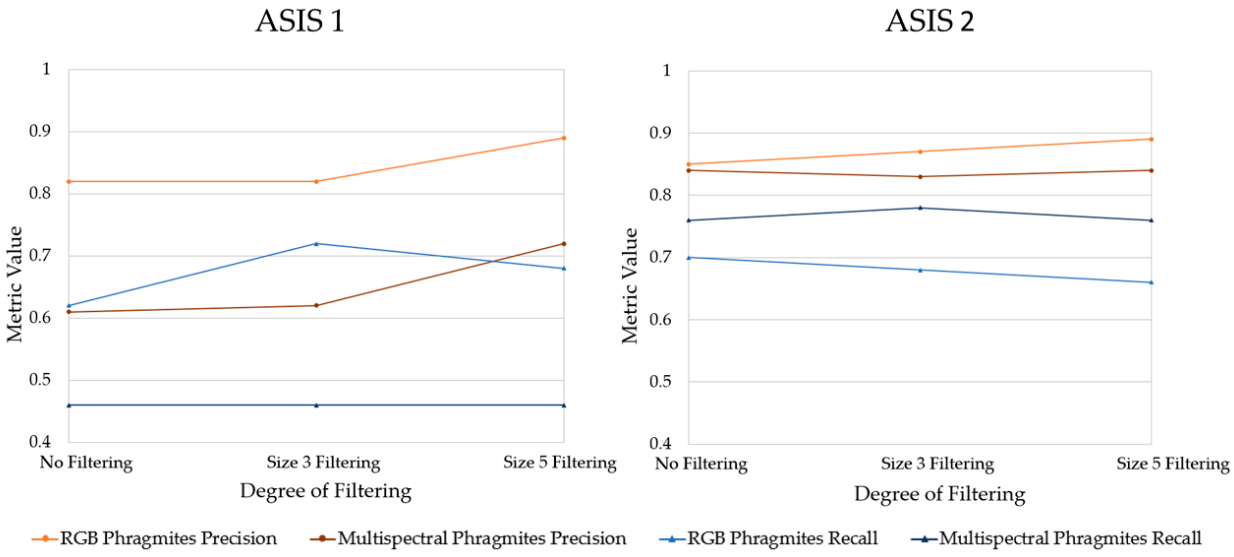

Figure 11. *Phragmites* precision and *Phragmites* recall across degrees of filtering for the "best" Assateague (ASIS) site results (**ASIS 2**) and the "worst" ASIS site results (**ASIS 1**). A metric value closer to 1 indicates more reliable results. "Filtering" refers to a majority filter and "size" refers to the size of the filter in number of pixels.

4. Discussion

Our results were comparable to other UAS studies that classify *Phragmites* cover using traditional machine learning methods [8,11,45] but were outperformed by deep learning approaches [49]. Table 7 summarizes the tradeoffs we found between the two sensors.

Table 7. Summary of our findings from the RGB vs. multispectral sensor comparison. Note: the price listed was what we spent to acquire the sensors at the time of purchase. DHM = Dog Head Marsh. ASIS = Assateague Island.

RGB Sensor	Multispectral Sensor
More affordable (Ricoh GR II cost of around USD 600)	More expensive (MicaSense RedEdge-3 cost of around USD 5500, MicaSense Altum-PT cost of around USD 16,700)
Requires no in-field calibration	Requires in-field photo of calibration panel before and after each flight for reflectance correction (The panel must remain clean, which can be challenging in natural environments)
Flight times can be more flexible pending tolerance of shadows in imagery	Requires that flights be scheduled around solar noon for best reflectance results
Simpler SfM processing	SfM processing requires extra reflectance calibration steps
Lacks red edge and near-infrared information	Includes red edge and near-infrared information useful for discerning vegetated and unvegetated cover
Generally produced classified cover maps with similar (DHM) or better (ASIS) accuracy metrics	Generally produced classified cover maps with similar (DHM) or worse (ASIS) accuracy metrics
Has a relatively lower learning curve to use the technology (Requires less technical expertise and potential troubleshooting)	Has a relatively higher learning curve to use the technology (Requires more technical expertise and potential troubleshooting)

Unlike previous studies, our work focused on identifying trade-offs between RGB and multispectral sensors for mapping *Phragmites* using products made via SfM with practical applications in mind. We found the additional spectral information provided by multispectral sensors did not consistently produce better classification of *Phragmites* than an RGB sensor (DHM results vs. ASIS results) using simple classification schema with UAS data. This may be because, across the featureset scenarios, the vegetation index and DSM-related features were frequently identified as the most important features within each featureset and other features were of minimal importance (Figures 5 and 8). The additional information from the multispectral sensor was not deemed important by the algorithm relevant to the DSM-related and vegetation index features, and the largely important DSM-related and vegetation index features could be obtained from either sensor type. The importance of the DSM-related and vegetation index features makes sense intuitively. Visually, one can distinguish the lighter senescing *Phragmites* leaves and relatively uniquely colored plumes from the surrounding vegetation (Figure 4). If the color distinction in senescing *Phragmites*' leaves and plumes are discernable by the human eye, it is unsurprising that vegetation indices used to detect vegetation health and greenness would be useful in image classification. The tall reed structure of *Phragmites* stands can also be visually distinguished from surrounding shorter vegetation in DSMs (Figure 4) and has a rougher surface, caused by the spaces between the tall reeds and plumes, than smooth pavement or other more uniform surfaces such as shorter homogeneous patches of herbaceous cover. However, as mentioned previously, the spectral information is still needed to differentiate *Phragmites* stands from other vegetation of similar height such as surrounding shrub cover.

The proper use of a multispectral sensor requires additional effort compared with RGB data collection. Use of a calibration panel—which must be kept clean through the duration of the survey (challenging in windy coastal environments)—is required for accurate reflectance measurements. The calibration panel enables precise compensation for changes in ambient lighting conditions that may occur throughout the duration of a flight. Ideally, images of the calibration panel are taken directly before and after multispectral data collection to provide the data required for the compensation in the reflectance data. The required timing of multispectral sensor flights around solar noon can be limiting if the area is influenced by tides; low tide imagery allows for the greatest subaerial extent of coverage and is often preferable when surveying coastal settings to maximize landscape data collection. A multispectral sensor may still be preferable to RGB when there is interest in monitoring vegetation health via an index like NDVI. GLI, which can be calculated without near-infrared data, was meant to identify green vegetation in imagery and has not necessarily been linked to vegetation health. There are other RGB vegetation indices available (e.g., [69]), but a multispectral sensor is more versatile and can enable additional spectral analyses post-data collection if the project needs to change. Regardless of the type of spectral data, it is worthwhile to calculate a vegetation index and collect imagery with sufficient overlap so SfM can provide elevation data that can be included in the featureset for classification, as including both these data leads to more reliable results (Tables 4 and 6), and they are typically identified by our RF algorithms as important features for higher quality classification results (Figures 5 and 8). However, NDVI was consistently identified as a top important feature across the ASIS multispectral results, while GLI was not consistently identified as important, and was often less important than the "red" feature, across the ASIS RGB results (Figure 8). This suggests NDVI may generalize more effectively than GLI across sites for classification purposes.

We found providing "All Uncorrelated Features" featuresets to the classification algorithm generally produced comparable or more reliable results for mapping *Phragmites* than featuresets containing correlated features, like the "All Features" featureset (Tables 4 and 6). The caveat, however, was the uncorrelated featureset still needed to include DSM-related features. When we added the DSM feature back into the uncorrelated featureset at ASIS site 2, the classification accuracy metrics consistently improved relative to the original "All Uncorrelated Features" results (Table 6). This provided further evidence of the advantage of including elevation information for mapping *Phragmites*.

We found smoothing does help reduce the salt-and-pepper effect to make the results more visually interpretable. However, due to the tall and thin reed structure of *Phragmites*, smoothing can remove small areas of *Phragmites* properly classified as *Phragmites* cover. This is potentially problematic for those developing treatment plans for the species, who are interested in where *Phragmites* individuals are appearing separate from the main stands, as individuals can indicate where the spread will continue (personal communication Jonathan Chase, National Park Service, October 2022).

Accuracy metrics varied across the ASIS sites (Figure 7). Future work can delve into possible explanations for this variation, such as different land cover distributions across the sites, different feature-value distributions (for example, whether elevation values varied across sites), or if varying weather and lighting conditions matter. For example, ASIS site 2, the "best" of the ASIS site classified results, was flown on a cloudy day before an afternoon storm. Perhaps the more diffused lighting conditions led to better classification results. Such different lighting and site characteristics may also explain the inconsistently identified important features across the ASIS sites (Figure 8). The "red" feature may have been identified as an important feature at ASIS (Figure 8) as unhealthy vegetation reflects more red light [72], which may have helped distinguish between the various degrees of senescing vegetation types at ASIS. More work is needed to understand why the "red" feature was not similarly identified as important in the "all uncorrelated features" workflows at the DHM (Supplementary Materials "DHM_pilotStudy_RGB_and_multispectral_PhragmitesMapping.html"). Wind, specifically, could be a variable impacting the classification results, as wind can result in

blurry orthomosaics (see Figure 4 for an example of "blurred" vegetation in panel B) and inaccurate vegetated surface elevations as the moving vegetation is not captured well via SfM. The underlying topography of each site could have also impacted the efficacy of the classification, specifically related to the DSM-derived features. Increased relief across a vegetated landscape means that shorter vegetation species on hills, like dunes, can reach the same surface height as taller vegetation, like *Phragmites*, located in lower-lying areas. When a site has low relief (i.e. relatively flat), the vegetated surface modeled in the DSM is a more direct indicator of relative vegetation height, and thus, taller species can be identified from the shorter species (as seen in Figure 4C). If species exist across a site with higher relief, there is a less clear distinction in the DSM between shorter and taller species useful for identifying *Phragmites*. More work is needed to examine how varying degrees of relief across sites, along with the distribution of *Phragmites* across the site, impacts the classification efficacy. Future work could also explore applying the untested workflows from the pilot study to the additional sites to examine their generalizability and evaluate whether results provide any insight into the across-site performance variation. Regardless of the workflow, future fieldwork efforts should be planned to take place during the *Phragmites* senescing period, as its spectral signature is more distinguishable from other vegetation at that time [33].

Based on our results, we can offer some hypotheses as to where these methods would be likely and unlikely to generalize. The work herein tests the approach at salt marsh (DHM) and barrier island (ASIS) settings. We anticipate that this approach would translate to another salt marsh setting given both the RGB and multispectral sensors produced usable results. Additional work is needed, however, to determine what site conditions or modifications to the workflow are necessary to consistently perform well at barrier island sites (e.g., topographic conditions, lighting conditions, low/no wind, etc.). Importantly, the methods herein are unlikely to perform well in more forested wetlands where underlying *Phragmites* is obscured by tree species. SfM would be unable to penetrate a forested canopy, leaving the underlying *Phragmites* undetected.

Now that we have methodologically identified important features and demonstrated they can provide useful *Phragmites* classification results, these features can be tested in other methods, such as deep learning approaches [49,81] and object-based classification workflows [8]. Object-based workflows using a sufficiently fine segmentation may be able to provide more reliable maps of locations of *Phragmites* individuals, as such results may not need to be smoothed to be visually interpretable. More work is needed to determine tradeoffs between object-based vs. pixel-based workflows.

SfM does pose limitations in densely vegetated areas and inundated areas. Specific site conditions must be met for SfM to model bathymetry in inundated areas, including clear, shallow water with low surface turbulence [82]. If these conditions are not met, the bathymetry results from SfM can be unreliable, as the camera is unable to penetrate the turbid water's surface and significant "holes" and local distortions in the DSM can occur from surface water turbulence. Even if these conditions are met, the effects of refraction through the water's surface require that inundated areas of SfM-produced DSMs be corrected for accuracy [50,82]. Bathymetric LiDAR systems can more reliably model bathymetry, e.g., providing penetration of at least two times the Secchi depth [83,84], which is the depth of water beyond which a high-contrast pattern on a submerged disk is no longer visible. This penetration is an advantage over SfM, which is heavily reliant on a lack of water turbidity.

Visual inspection of the DHM and ASIS DSMs verified that some distortions were present in the inundated areas of the models used to produce the results herein (see DSMs available in [59,78]), but we had insufficient ground reference data to verify whether the bathymetry was reliably modeled as it was outside the scope of our vegetation mapping goals. Such distortions in the inundated areas of the DSMs could have impacted our classification results by introducing outliers in the DSM-related feature values for the "not vegetation" class, as water was included in this class. However, our high evaluation metrics for the "not vegetation" class suggest that these impacts were minimal if present

(Supplementary Materials S9, S10, S12 and S13). LiDAR sensors have the potential to provide more consistently accurate "not vegetation" DSM-related feature values for the classification and may prove useful in projects where it is important to monitor changes in topography and bathymetry in addition to monitoring invasive species cover. However, a refraction correction for underwater points collected via LiDAR is still needed to achieve maximum accuracy [83,84].

In addition to the limitations of SfM regarding inundated areas, SfM models the surface topography of a site that is visible to the camera, including the surface of the vegetation canopy. Therefore, the DSM values represent vegetated surface elevations rather than vegetation heights. There are techniques for filtering sparser vegetation to create estimated DEMs from DSMs, but these approaches are limited in densely vegetated environments [51,52]. In addition, SfM can fail to resolve the tall, thin, and therefore difficult to detect, tops of reeds like *Phragmites*, particularly if they are blowing in the wind and, therefore, the relevant points have higher uncertainty associated with them in the SfM process. This can lead to underestimation of such species' surface heights. Such effects likely occurred in our processing despite taking steps to use less aggressive point filtering techniques, as indicated by our comparison of DSM vegetation surface elevations compared to in-field vegetation height measurements that showed *Phragmites* surface elevation tended to be underestimated (Supplementary Materials S8). Though the DSM-related features were consistently identified as important across classification workflow iterations, this underestimation of *Phragmites*' surface elevation may have impacted the DSM-related features' efficacy, such as their ability to discern *Phragmites* from shorter and/or less rough mixed in and surrounding vegetation.

UAS LiDAR with its active laser-based data collection may better capture the surface height and structure of vegetation than SfM and improve the classification results. A canopy height model could be used as another feature if LiDAR data were collected, as the multiple returns can be processed to obtain vegetation height rather than vegetation surface elevation. Such data may help differentiate between shorter "other vegetation" on higher terrain elevations like dunes from taller *Phragmites* in lower laying marsh terrain (Figure 6). The consistent relatively high importance assigned to the DSM-related features throughout the work herein lends to the hypothesis that a more nuanced structural metric, such as canopy height model values, would improve the classification results. However, a LiDAR system would increase various costs of the approach—both technical and financial.

More work is needed to determine if the methods herein provide reliable cover maps for other species and if the same features are identified as important. For example, the physical structure of *Phragmites*, a tall reed, may explain why DSM-related features were deemed important relative to other features in its classification. Such features may also be important for species with similar physical traits, such as the tall *Fallopia japonica* ("Japanese knotweed") that also grows in stands. The tested classification workflows herein may transfer to other similar tall, reed-like invasive species, such as *Fallopia japonica*, without much modification—particularly if the species has similar senescing traits as *Phragmites*, such as plumes or lightened color relative to the surrounding vegetation. However, DSM-related features may not be as important to differentiate other species of interest. For example, the invasive wetland species *Lythrum salicaria* ("purple loosestrife") is a species that has reddish-purple stems and flowers. Its unique physical traits are not so much its height but its colorful blooms. If the methods herein were applied to work that used a classification schema of "not vegetation", "other vegetation", and "purple loosestrife", we may find the multispectral sensor outperforms RGB as the additional spectral features may prove important in identifying this species given its color. Additional work is needed to conduct similar method comparison studies for other invasive species and explore such hypotheses.

Adaptive management is an approach to ecological restoration that requires monitoring post-restoration to verify that the restored site remains on the desired recovery trajectory, as well as provide learned information to make more effective restoration plans

in the future [85–87]. For adaptive management to be successfully implemented, such as the management and eradication of invasive species, monitoring sites before restoration and over time is essential to be able to react to and learn from any changes in site conditions (e.g., *Phragmites* re-establishing after initial eradication). However, resources like time, cost, staffing, and staff training are often seen as limitations to implementing adaptive management [85].

UAS workflows are rapid monitoring techniques that can provide a snapshot of conditions across an entire site to support ecological restoration strategies, like adaptive management, complementary to other monitoring approaches. Knowing the trade-offs (resource requirements, efficiency, and efficacy) between workflows and nuances of sensor types can help identify where it may be best applied in ecological management applications. Specifically, understanding where a multispectral sensor over an RGB sensor is required can help to inform how practitioners may prioritize or invest with limited monitoring resources. In addition, the essence of the workflow used herein that consists of creating reference datasets, creating featuresets, training and testing a random forest, and evaluating the classified results can be replicated in GIS software. The GIS applicability was intentional so that workflows could be accessible to those who may not have coding skills but could use the graphical user interface of the software.

5. Conclusions

We have demonstrated that UAS RGB and multispectral imagery can each provide useful invasive species cover maps. We did not find a statistically significant difference between the RGB and multispectral results per comparing KHAT values via the Z statistic following [63] (pp. 127–132). The best classification results were achieved when information from both the orthomosaic and the DSM were included in the featureset used in the classification workflow. The classification workflow did transfer from the pilot study site to additional study sites. However, the reliability of the cover maps across the additional sites varied, and additional research is needed to understand why. By leveraging experiment design intended for method comparisons, rather than comparing different species classification studies in hindsight, we can better understand the data and methods required for usable classification results and begin to capture how these may, or may not, vary by species. Additional work is needed to explore which features, whether structural- or spectral-based, are more likely to provide the necessary distinction between future classes and explore practical methods.

Supplementary Materials: The following supporting information can be downloaded at https://www.mdpi.com/article/10.3390/rs16244691/s1, SI 1: Aeropoint Survey Accuracy; SI 2: Additional Flight Information for the Dog Head Marsh Site; SI 3: Additional Details on SfM Processing; SI 4: Supporting Equations for Reference Data Sampling and Feature Creation; SI 5: Comparison of KHAT statistics at Dog Head Marsh; SI 6: Details on Differences between DHM and ASIS Fieldwork and Processing; SI 7: Reference Data Distributions Across Classes for ASIS Sites; SI 8: Vertical DSM Errors Based on Surveyed Unmarked Validation Points and Vegetation Heights Measured in the Field; SI 9: Dog Head Marsh Error Matrices for the "Best" Classified Results; SI 10: Thematic Accuracy Metric Reports for Dog Head Marsh; SI 11: Table of Thematic Evaluation Metrics for the ASIS Sites; SI 12: Thematic Accuracy Metric Reports for ASIS Sites; SI 13: Error Matrices for ASIS Sites; SI 14: Classified LC Maps from both sensors for all ASIS Sites; SI 15: Comparison of KHAT statistics for ASIS sites 1 & 2; SI 16: Accuracy Metrics from Smoothed ASIS Results. Rendered Jupyter notebooks of the code used for the analyses herein are available in the supporting information as files to provide methods transparency: ASIS_multispectral_PhragmitesMapping.html (Details for the ASIS sites: how the imagery data was processed in preparation for the classification workflows, and the multispectral-based classifications and evaluation of result accuracy); ASIS_RGB_PhragmitesMapping.html (Details for the ASIS sites: how the imagery data was processed in preparation for the classification workflows, and the RGB-based classifications and evaluation of result accuracy); ASIS_sites1and2_smoothingEffects.html (Details how the smoothing was performed on the ASIS 1 and 2 classified results, along with the recalculation of the accuracy metric reports for

the smoothed results); DHM_pilotStudy_RGB_and_multispectral_PhragmitesMapping.html (Details for the DHM pilot study site: how the imagery data was processed in preparation for the classification workflows, the analysis of the DSM vertical errors, the RGB-based classifications and evaluation of result accuracy, and the multispectral-based classifications and evaluation of result accuracy); KHATcalculations.html (Details the calculation of the Z statistic for comparing two independent matrices for the DHM results and then for ASIS sites 1 and 2). Please note that all file paths in the html files have been replaced with "user_input_path_string". Other credentials have also been replaced with "redacted". References [50,60,62,63,88–90] are cited in the Supplementary Materials.

Author Contributions: A.D.E.: Conceptualization, Data curation, Formal analysis, Funding acquisition, Investigation, Methodology, Project administration, Software, Resources, Visualization, Validation, Writing—original draft. J.C.: Conceptualization, Data curation, Formal analysis, Investigation, Methodology, Validation, Writing—review and editing. V.S.: Conceptualization, Data curation, Formal analysis, Investigation, Methodology, Validation, Writing—review and editing. E.L.: Conceptualization, Formal analysis, Funding acquisition, Investigation, Methodology, Project administration, Validation, Resources, Writing—original draft. All authors have read and agreed to the published version of the manuscript.

Funding: This work was supported by the USGS Coastal and Marine Hazards and Resources Program as part of the Future Landscape Adaptation and Coastal Change project.

Data Availability Statement: The field data, orthomosaics, and DSMs for the DHM and ASIS can be found in the following USGS data releases: https://doi.org/10.5066/P9W8JS7P, https://doi.org/10.5066/P916LRZN.

Acknowledgments: We would like to extend our gratitude to the Waquoit Bay National Estuarine Research Reserve for providing access to the Dog Head Marsh study site. We would also like to thank our partners at Assateague Island National Seashore for providing access to the ASIS study sites as well as support in field efforts, particularly Jonathan Chase who joined us in the field to collect vegetation data. The Aerial Imaging and Mapping Group (Sandra Brosnahan, Seth Ackerman, Jin-Si Over, and Elizabeth Pendelton, also including author Jennifer Cramer) at the USGS Woods Hole Coastal and Marine Science Center collected the UAS imagery for this study and helped collect ground reference data at the DHM and ASIS sites. Others at the USGS Woods Hole Coastal and Marine Science Center we would like to thank include Allyson Boggess and Sydney Nick, who helped collect vegetation data at the DHM study site. The USGS National Uncrewed Systems Office provided support for field efforts at the DHM and for image processing. We would like to thank Richard Signell for his support in coding the analyses for this work and connecting us with the resources provided by Earth Science Information Partners (ESIP). We also thank ESIP for providing computational resources. Zachary Jablons provided support in de-bugging the code and answering questions about Python and cloud computing. Much of this work was conducted while Evans was employed at Woods Hole Oceanographic Institution, and we would like to thank Andrew Ashton in the Department of Geology and Geophysics for his support. Lastly, we would like to thank our internal USGS reviewers, Chris Sherwood and Joshua von Nonn, and the four anonymous peer reviewers who improved the quality of this manuscript. Any use of trade, firm, or product names is for descriptive purposes only and does not imply endorsement by the U.S. Government.

Conflicts of Interest: The authors declare no conflicts of interest.

References

1. Joyce, K.E.; Anderson, K.; Bartolo, R.E. Of Course We Fly Unmanned—We're Women! *Drones* **2021**, *5*, 21. [CrossRef]
2. Anderson, K.; Gaston, K.J. Lightweight Unmanned Aerial Vehicles Will Revolutionize Spatial Ecology. *Front. Ecol. Environ.* **2013**, *11*, 138–146. [CrossRef]
3. Anderson, C.J.; Heins, D.; Pelletier, K.C.; Bohnen, J.L.; Knight, J.F. Mapping Invasive Phragmites Australis Using Unoccupied Aircraft System Imagery, Canopy Height Models, and Synthetic Aperture Radar. *Remote Sens.* **2021**, *13*, 3303. [CrossRef]
4. Marcaccio, J.V.; Chow-Fraser, P. Mapping Options to Track Invasive Phragmites Australis in the Great Lakes Basin in Canada. In *Water Resources and Wetlands*; Gastescu, P., Bretcan, P., Eds.; Romanian Limnogeographical Association: Dambovita, Romania, 2016; pp. 75–82.
5. Dronova, I.; Kislik, C.; Dinh, Z.; Kelly, M. A Review of Unoccupied Aerial Vehicle Use in Wetland Applications: Emerging Opportunities in Approach, Technology, and Data. *Drones* **2021**, *5*, 45. [CrossRef]
6. Huylenbroeck, L.; Laslier, M.; Dufour, S.; Georges, B.; Lejeune, P.; Michez, A. Using Remote Sensing to Characterize Riparian Vegetation: A Review of Available Tools and Perspectives for Managers. *J. Environ. Manag.* **2020**, *267*, 110652. [CrossRef]

7. Rodríguez-González, P.M.; Albuquerque, A.; Martínez-Almarza, M.; Díaz-Delgado, R. Long-Term Monitoring for Conservation Management: Lessons from a Case Study Integrating Remote Sensing and Field Approaches in Floodplain Forests. *J. Environ. Manag.* **2017**, *202*, 392–402. [CrossRef]
8. Brooks, C.; Weinstein, C.; Poley, A.; Grimm, A.; Marion, N.; Bourgeau-Chavez, L.; Hansen, D.; Kowalski, K. Using Uncrewed Aerial Vehicles for Identifying the Extent of Invasive Phragmites Australis in Treatment Areas Enrolled in an Adaptive Management Program. *Remote Sens.* **2021**, *13*, 1895. [CrossRef]
9. Ajamian, C.; Chang, H.-C.; Tomkins, K.; Farebrother, W.; Heim, R.; Rahman, S. Identifying Invasive Weed Species in Alpine Vegetation Communities Based on Spectral Profiles. *Geomatics* **2021**, *1*, 177–191. [CrossRef]
10. Papp, L.; Van Leeuwen, B.; Szilassi, P.; Tobak, Z.; Szatmári, J.; Árvai, M.; Mészáros, J.; Pásztor, L. Monitoring Invasive Plant Species Using Hyperspectral Remote Sensing Data. *Land* **2021**, *10*, 29. [CrossRef]
11. Abeysingh, T.; Simic Milas, A.; Arend, K.; Hohman, B.; Reil, P.; Gregory, A.; Vázquez-Ortega, A. Mapping Invasive Phragmites Australis in the Old Woman Creek Estuary Using UAV Remote Sensing and Machine Learning Classifiers. *Remote Sens.* **2019**, *11*, 1380. [CrossRef]
12. Hazelton, E.L.; Mozdzer, T.J.; Burdick, D.M.; Kettenring, K.M.; Whigham, D.F. Phragmites Australis Management in the United States: 40 Years of Methods and Outcomes. *AoB Plants* **2014**, *6*, plu001. [CrossRef] [PubMed]
13. Chambers, R.M.; Meyerson, L.A.; Saltonstall, K. Expansion of Phragmites Australis into Tidal Wetlands of North America. *Aquat. Bot.* **1999**, *64*, 261–273. [CrossRef]
14. McCormick, M.K.; Whigham, D.F.; Stapp, J.R.; Hazelton, E.L.; McFarland, E.K.; Kettenring, K.M. Shoreline Modification Affects Recruitment of Invasive Phragmites Australis. *Wetl. Ecol. Manag.* **2020**, *28*, 909–919. [CrossRef]
15. Smith, J.A. The Role of Phragmites Australis in Mediating Inland Salt Marsh Migration in a Mid-Atlantic Estuary. *PLoS ONE* **2013**, *8*, e65091. [CrossRef]
16. Chambers, R.M.; Havens, K.J.; Killeen, S.; Berman, M. Common Reed Phragmites Australis Occurrence and Adjacent Land Use Along Estuarine Shoreline in Chesapeake Bay. *Wetlands* **2008**, *28*, 1097–1103. [CrossRef]
17. Tully, K.; Gedan, K.; Epanchin-Niell, R.; Strong, A.; Bernhardt, E.S.; BenDor, T.; Mitchell, M.; Kominoski, J.; Jordan, T.E.; Neubauer, S.C.; et al. The Invisible Flood: The Chemistry, Ecology, and Social Implications of Coastal Saltwater Intrusion. *BioScience* **2019**, *69*, 368–378. [CrossRef]
18. Cook, C.E.; McCluskey, A.M.; Chambers, R.M. Impacts of Invasive Phragmites Australis on Diamondback Terrapin Nesting in Chesapeake Bay. *Estuaries Coasts* **2018**, *41*, 966–973. [CrossRef]
19. Hunter, K.L.; Fox, D.A.; Brown, L.M.; Able, K.W. Responses of Resident Marsh Fishes to Stages of Phragmites Australis Invasion in Three Mid Atlantic Estuaries. *Estuaries Coasts* **2006**, *29*, 487–498. [CrossRef]
20. Able, K.W.; Hagan, S.M. Impact of Common Reed, Phragmites Australis, on Essential Fish Habitat: Influence on Reproduction, Embryological Development, and Larval Abundance of Mummichog (*Fundulus heteroclitus*). *Estuaries* **2003**, *26*, 40–50. [CrossRef]
21. Benoit, L.K.; Askins, R.A. Impact of the Spread of Phragmites on the Distribution of Birds in Connecticut Tidal Marshes. *Wetlands* **1999**, *19*, 194–208. [CrossRef]
22. Sheng, Y.P.; Rivera-Nieves, A.A.; Zou, R.; Paramygin, V.A.; Angelini, C.; Sharp, S.J. Invasive Phragmites Provides Superior Wave and Surge Damage Protection Relative to Native Plants during Storms. *Environ. Res. Lett.* **2021**, *16*, 054008. [CrossRef]
23. Rooth, J.E.; Stevenson, J.C.; Cornwell, J.C. Increased Sediment Accretion Rates Following Invasion by Phragmites Australis: The Role of Litter. *Estuaries* **2003**, *26*, 475–483. [CrossRef]
24. Walter, M.; Mondal, P. Mapping of Phragmites in Estuarine Wetlands Using High-Resolution Aerial Imagery. *Environ. Monit. Assess.* **2023**, *195*, 478. [CrossRef] [PubMed]
25. Rupasinghe, P.A.; Chow-Fraser, P. Mapping Phragmites Cover Using WorldView 2/3 and Sentinel 2 Images at Lake Erie Wetlands, Canada. *Biol. Invasions* **2021**, *23*, 1231–1247. [CrossRef]
26. Oteman, B.; Scrieciu, A.; Bouma, T.J.; Stanica, A.; van der Wal, D. Indicators of Expansion and Retreat of Phragmites Based on Optical and Radar Satellite Remote Sensing: A Case Study on the Danube Delta. *Wetlands* **2021**, *41*, 72. [CrossRef]
27. Long, A.L.; Kettenring, K.M.; Hawkins, C.P.; Neale, C.M. Distribution and Drivers of a Widespread, Invasive Wetland Grass, Phragmites Australis, in Wetlands of the Great Salt Lake, Utah, USA. *Wetlands* **2017**, *37*, 45–57. [CrossRef]
28. Xie, Y.; Zhang, A.; Welsh, W. Mapping Wetlands and Phragmites Using Publically Available Remotely Sensed Images. *Photogramm. Eng. Remote Sens.* **2015**, *81*, 69–78. [CrossRef]
29. Bourgeau-Chavez, L.L.; Kowalski, K.P.; Mazur, M.L.C.; Scarbrough, K.A.; Powell, R.B.; Brooks, C.N.; Huberty, B.; Jenkins, L.K.; Banda, E.C.; Galbraith, D.M.; et al. Mapping Invasive Phragmites Australis in the Coastal Great Lakes with ALOS PALSAR Satellite Imagery for Decision Support. *J. Great Lakes Res.* **2013**, *39*, 65–77. [CrossRef]
30. Lantz, N.J.; Wang, J. Object-Based Classification of Worldview-2 Imagery for Mapping Invasive Common Reed, Phragmites Australis. *Can. J. Remote Sens.* **2013**, *39*, 328–340. [CrossRef]
31. Laba, M.; Blair, B.; Downs, R.; Monger, B.; Philpot, W.; Smith, S.; Sullivan, P.; Baveye, P.C. Use of Textural Measurements to Map Invasive Wetland Plants in the Hudson River National Estuarine Research Reserve with IKONOS Satellite Imagery. *Remote Sens. Environ.* **2010**, *114*, 876–886. [CrossRef]
32. Laba, M.; Downs, R.; Smith, S.; Welsh, S.; Neider, C.; White, S.; Richmond, M.; Philpot, W.; Baveye, P. Mapping Invasive Wetland Plants in the Hudson River National Estuarine Research Reserve Using Quickbird Satellite Imagery. *Remote Sens. Environ.* **2008**, *112*, 286–300. [CrossRef]

33. Gilmore, M.S.; Wilson, E.H.; Barrett, N.; Civco, D.L.; Prisloe, S.; Hurd, J.D.; Chadwick, C. Integrating Multi-Temporal Spectral and Structural Information to Map Wetland Vegetation in a Lower Connecticut River Tidal Marsh. *Remote Sens. Environ.* **2008**, *112*, 4048–4060. [CrossRef]
34. Pengra, B.W.; Johnston, C.A.; Loveland, T.R. Mapping an Invasive Plant, Phragmites Australis, in Coastal Wetlands Using the EO-1 Hyperion Hyperspectral Sensor. *Remote Sens. Environ.* **2007**, *108*, 74–81. [CrossRef]
35. Philipp, K.R.; Field, R.T. Phragmites Australis Expansion in Delaware Bay Salt Marshes. *Ecol. Eng.* **2005**, *25*, 275–291. [CrossRef]
36. Mcleod, G.M.; Daigneau, J.; Gucwa, R.J. Supervised Classification of Landsat-7 Imagery for the Detection of Phragmites Australis in Back Bay National Wildlife Refuge. *J. North Carol. Acad. Sci.* **2005**, *121*, 61–70.
37. Maheu-Giroux, M.; de Blois, S. Mapping the Invasive Species Phragmites Australis in Linear Wetland Corridors. *Aquat. Bot.* **2005**, *83*, 310–320. [CrossRef]
38. Arzandeh, S.; Wang, J. Monitoring the Change of Phragmites Distribution Using Satellite Data. *Can. J. Remote Sens.* **2003**, *29*, 24–35. [CrossRef]
39. Ozbay, G.; Augustine, A.; Fletcher, R. Remote Sensing of Phragmites Australis Invasion in Delaware Tidal Marsh Zones: Issues to Consider. *J. Geophys. Remote Sens.* **2003**, *1*, 1–3.
40. Lade, K.P. *Delineation and Classification of Phragmites Communis (Common Reed) by Interpretation of Aerial Photography and SPOT Satellite Multispectral and Panchromatic Digital Data*; National Oceanic and Atmospheric Administration: Washington, DC, USA, 1988.
41. Ramsey, E.W., III; Rangoonwala, A. *Mapping the Change of Phragmites Australis Live Biomass in the Lower Mississippi River Delta Marshes*; US Geological Survey: Reston, VA, USA, 2017.
42. Suir, G.M.; Saltus, C.L.; Reif, M.K. *Geospatial Assessments of Phragmites Australis Die-Off in South Louisiana: Preliminary Findings*; U.S. Army Engineer Research and Development Center: Lafayette, LA, USA, 2018.
43. Ludwig, D.F.; Iannuzzi, T.J.; Esposito, A.N. Phragmites and Environmental Management: A Question of Values. *Estuaries* **2003**, *26*, 624–630. [CrossRef]
44. Mohler, R.L.; Morse, J.M. Using UAV Imagery to Map Invasive Phragmites Australis on the Crow Island State Game Area, Michigan, USA. *Wetl. Ecol. Manag.* **2022**, *30*, 1213–1229. [CrossRef]
45. Zaman, B.; McKee, M. Smart Tools for Wetland Management: UAV Data and Artificial Intelligence Technique for Change Detection of Phragmites Australis in the Bear River Migratory Bird Refuge. *Appl. Ecol. Environ. Sci.* **2020**, *8*, 387–395.
46. Casagrande, L.; Machado, G.M.; Samiappan, S.; Turnage, G.; Hathcock, L.; Moorhead, R. Probabilistic Neural Network and Wavelet Transform for Mapping of Phragmites Australis Using Low Altitude Remote Sensing. In Proceedings of the 2017 30th SIBGRAPI Conference on Graphics, Patterns and Images (SIBGRAPI), Niterói, Brazil, 17–20 October 2017; pp. 269–276.
47. Samiappan, S.; Turnage, G.; Hathcock, L.A.; Moorhead, R. Mapping of Invasive Phragmites (Common Reed) in Gulf of Mexico Coastal Wetlands Using Multispectral Imagery and Small Unmanned Aerial Systems. *Int. J. Remote Sens.* **2017**, *38*, 2861–2882. [CrossRef]
48. Zaman, B.; Jensen, A.M.; McKee, M. Use of High-Resolution Multispectral Imagery Acquired with an Autonomous Unmanned Aerial Vehicle to Quantify the Spread of an Invasive Wetlands Species. In Proceedings of the 2011 IEEE International Geoscience and Remote Sensing Symposium, Vancouver, BC, Canada, 24–29 July 2011; pp. 803–806.
49. Higgisson, W.; Cobb, A.; Tschierschke, A.; Dyer, F. Estimating the Cover of Phragmites Australis Using Unmanned Aerial Vehicles and Neural Networks in a Semi-Arid Wetland. *River Res. Appl.* **2021**, *37*, 1312–1322. [CrossRef]
50. Woodget, A.S.; Dietrich, J.T.; Wilson, R.T. Quantifying Below-Water Fluvial Geomorphic Change: The Implications of Refraction Correction, Water Surface Elevations, and Spatially Variable Error. *Remote Sens.* **2019**, *11*, 2415. [CrossRef]
51. Anders, N.; Valente, J.; Masselink, R.; Keesstra, S. Comparing Filtering Techniques for Removing Vegetation from UAV-Based Photogrammetric Point Clouds. *Drones* **2019**, *3*, 61. [CrossRef]
52. DeWitt, J.D.; Warner, T.A.; Chirico, P.G.; Bergstresser, S.E. Creating High-Resolution Bare-Earth Digital Elevation Models (DEMs) from Stereo Imagery in an Area of Densely Vegetated Deciduous Forest Using Combinations of Procedures Designed for Lidar Point Cloud Filtering. *GIScience Remote Sens.* **2017**, *54*, 552–572. [CrossRef]
53. Jochems, L.W.; Brandt, J.; Monks, A.; Cattau, M.; Kolarik, N.; Tallant, J.; Lishawa, S. Comparison of Different Analytical Strategies for Classifying Invasive Wetland Vegetation in Imagery from Unpiloted Aerial Systems (UAS). *Remote Sens.* **2021**, *13*, 4733. [CrossRef]
54. Lu, T.; Wan, L.; Qi, S.; Gao, M. Land Cover Classification of UAV Remote Sensing Based on Transformer–CNN Hybrid Architecture. *Sensors* **2023**, *23*, 5288. [CrossRef]
55. Khan, M.; Hanan, A.; Kenzhebay, M.; Gazzea, M.; Arghandeh, R. Transformer-Based Land Use and Land Cover Classification with Explainability Using Satellite Imagery. *Sci. Rep.* **2024**, *14*, 16744. [CrossRef]
56. Yao, J.; Zhang, B.; Li, C.; Hong, D.; Chanussot, J. Extended Vision Transformer (ExViT) for Land Use and Land Cover Classification: A Multimodal Deep Learning Framework. *IEEE Trans. Geosci. Remote Sens.* **2023**, *61*, 5514415. [CrossRef]
57. Tan, C.; Sun, F.; Kong, T.; Zhang, W.; Yang, C.; Liu, C. A Survey on Deep Transfer Learning. In *Artificial Neural Networks and Machine Learning–ICANN 2018, Proceedings of the 27th International Conference on Artificial Neural Networks, Rhodes, Greece, 4–7 October 2018, Part III 27*; Springer: Berlin/Heidelberg, Germany, 2018; pp. 270–279.
58. Buscombe, D.; Goldstein, E.B.; Sherwood, C.R.; Bodine, C.; Brown, J.A.; Favela, J.; Fitzpatrick, S.; Kranenburg, C.J.; Over, J.; Ritchie, A.C.; et al. Human-in-the-Loop Segmentation of Earth Surface Imagery. *Earth Space Sci.* **2022**, *9*, e2021EA002085. [CrossRef]

59. Cramer, J.M.; Scholl, V.M.; Evans, A.D.; Ackerman, S.D.; Pendleton, E.A.; Brosnahan, S.M.; Nick, S.K.; Boggess, A.A. *Topographic and Multispectral Reflectance Products, Aerial Imagery, Ground Spectra, Vegetation, and Associated GPS Data Collected During Uncrewed Aircraft System (UAS) Operations—Dog Head Marsh at South Cape Beach, Mashpee, MA, October 7–8, 2021*; U.S. Geological Survey Data Release: Reston, VA, USA, 2024. [CrossRef]
60. Over, J.-S.R.; Ritchie, A.C.; Kranenburg, C.J.; Brown, J.A.; Buscombe, D.D.; Noble, T.; Sherwood, C.R.; Warrick, J.A.; Wernette, P.A. *Processing Coastal Imagery with Agisoft Metashape Professional Edition, Version 1.6—Structure from Motion Workflow Documentation*; US Geological Survey: Reston, VA, USA, 2021.
61. Agisoft Helpdesk Portal. Available online: https://agisoft.freshdesk.com/support/solutions/articles/31000148780-micasense-rededge-mx-processing-workflow-including-reflectance-calibration-in-agisoft-metashape-pro (accessed on 4 December 2024).
62. Meneses, N.C.; Baier, S.; Reidelstürz, P.; Geist, J.; Schneider, T. Modelling Heights of Sparse Aquatic Reed (Phragmites Australis) Using Structure from Motion Point Clouds Derived from Rotary-and Fixed-Wing Unmanned Aerial Vehicle (UAV) Data. *Limnologica* **2018**, *72*, 10–21. [CrossRef]
63. Congalton, R.G.; Green, K. *Assessing the Accuracy of Remotely Sensed Data: Principles and Practices*; CRC Press: Boca Raton, FL, USA, 2019.
64. Haralick, R.M.; Shanmugam, K.; Dinstein, I.H. Textural Features for Image Classification. *IEEE Trans. Syst. Man Cybern.* **1973**, *SMC-3*, 610–621. [CrossRef]
65. Grizonnet, M.; Michel, J.; Poughon, V.; Inglada, J.; Savinaud, M.; Cresson, R. Orfeo ToolBox: Open Source Processing of Remote Sensing Images. *Open Geospat. Data Softw. Stand.* **2017**, *2*, 15. [CrossRef]
66. HaralickTextureExtraction. Available online: https://www.orfeo-toolbox.org/CookBook/Applications/app_HaralickTextureExtraction.html (accessed on 4 December 2024).
67. Löfstedt, T.; Brynolfsson, P.; Asklund, T.; Nyholm, T.; Garpebring, A. Gray-Level Invariant Haralick Texture Features. *PLoS ONE* **2019**, *14*, e0212110. [CrossRef] [PubMed]
68. Louhaichi, M.; Borman, M.M.; Johnson, D.E. Spatially Located Platform and Aerial Photography for Documentation of Grazing Impacts on Wheat. *Geocarto Int.* **2001**, *16*, 65–70. [CrossRef]
69. Gitelson, A.A.; Kaufman, Y.J.; Stark, R.; Rundquist, D. Novel Algorithms for Remote Estimation of Vegetation Fraction. *Remote Sens. Environ.* **2002**, *80*, 76–87. [CrossRef]
70. Eng, L.S.; Ismail, R.; Hashim, W.; Baharum, A. The Use of VARI, GLI, and VIgreen Formulas in Detecting Vegetation in Aerial Images. *Int. J. Technol.* **2019**, *10*, 1385–1394. [CrossRef]
71. Rouse, J.W.; Haas, R.H.; Schell, J.A.; Deering, D.W. Monitoring Vegetation Systems in the Great Plains with ERTS. *NASA Spec. Publ* **1974**, *351*, 309.
72. Tucker, C.J. Red and Photographic Infrared Linear Combinations for Monitoring Vegetation. *Remote Sens. Environ.* **1979**, *8*, 127–150. [CrossRef]
73. Kubus, M. The Problem of Redundant Variables in Random Forests. *Acta Univ. Lodziensis. Folia Oeconomica* **2018**, *6*, 7–16. [CrossRef]
74. McKinney, W. Data Structures for Statistical Computing in Python. *SciPy* **2010**, *445*, 51–56.
75. Sheykhmousa, M.; Mahdianpari, M.; Ghanbari, H.; Mohammadimanesh, F.; Ghamisi, P.; Homayouni, S. Support Vector Machine versus Random Forest for Remote Sensing Image Classification: A Meta-Analysis and Systematic Review. *IEEE J. Sel. Top. Appl. Earth Obs. Remote Sens.* **2020**, *13*, 6308–6325. [CrossRef]
76. Pedregosa, F.; Varoquaux, G.; Gramfort, A.; Michel, V.; Thirion, B.; Grisel, O.; Blondel, M.; Prettenhofer, P.; Weiss, R.; Dubourg, V.; et al. Scikit-Learn: Machine Learning in Python. *J. Mach. Learn. Res.* **2011**, *12*, 2825–2830.
77. Pontius, R.G., Jr.; Millones, M. Death to Kappa: Birth of Quantity Disagreement and Allocation Disagreement for Accuracy Assessment. *Int. J. Remote Sens.* **2011**, *32*, 4407–4429. [CrossRef]
78. Cramer, J.M.; Evans, A.D.; Brosnahan, S.M.; Over, J.R.; Ackerman, S.D.; Lentz, E.E.; Hulslander, B. *Topographic and Multispectral Reflectance Products, Aerial Imagery, Spectral Reflectance Profiles, Vegetation Surveys, and Associated GPS Data Collected During Uncrewed Aircraft System (UAS) Operations—Assateague Island National Seashore, Maryland, 10–14 October 2022*; U.S. Geological Survey Data Release: Reston, VA, USA, 2023. [CrossRef]
79. Suir, G.M.; Wilcox, D.A.; Reif, M. Classification of Typha-Dominated Wetlands Using Airborne Hyperspectral Imagery along Lake Ontario, USA. *Aquat. Ecosyst. Health Manag.* **2021**, *24*, 140–155. [CrossRef]
80. Virtanen, P.; Gommers, R.; Oliphant, T.E.; Haberland, M.; Reddy, T.; Cournapeau, D.; Burovski, E.; Peterson, P.; Weckesser, W.; Bright, J.; et al. SciPy 1.0: Fundamental Algorithms for Scientific Computing in Python. *Nat. Methods* **2020**, *17*, 261–272. [CrossRef]
81. Cohen, J.G.; Lewis, M.J. Development of an Automated Monitoring Platform for Invasive Plants in a Rare Great Lakes Ecosystem Using Uncrewed Aerial Systems and Convolutional Neural Networks. In Proceedings of the 2020 international conference on unmanned aircraft systems (ICUAS), Athens, Greece, 1–4 September 2020; pp. 1553–1564.
82. Woodget, A.; Carbonneau, P.; Visser, F.; Maddock, I.P. Quantifying Submerged Fluvial Topography Using Hyperspatial Resolution UAS Imagery and Structure from Motion Photogrammetry. *Earth Surf. Process. Landf.* **2015**, *40*, 47–64. [CrossRef]
83. Szafarczyk, A.; Toś, C. The Use of Green Laser in LiDAR Bathymetry: State of the Art and Recent Advancements. *Sensors* **2022**, *23*, 292. [CrossRef]
84. Mandlburger, G.; Pfennigbauer, M.; Schwarz, R.; Flöry, S.; Nussbaumer, L. Concept and Performance Evaluation of a Novel UAV-Borne Topo-Bathymetric LiDAR Sensor. *Remote Sens.* **2020**, *12*, 986. [CrossRef]

85. Månsson, J.; Eriksson, L.; Hodgson, I.; Elmberg, J.; Bunnefeld, N.; Hessel, R.; Johansson, M.; Liljebäck, N.; Nilsson, L.; Olsson, C.; et al. Understanding and Overcoming Obstacles in Adaptive Management. *Trends Ecol. Evol.* **2023**, *38*, 55–71. [CrossRef] [PubMed]
86. Murray, C.; Marmorek, D. Adaptive Management and Ecological Restoration. *Ecol. Restor. Southwest. Ponder. Pine For.* **2003**, *2*, 417–428.
87. Thom, R.M. Adaptive Management of Coastal Ecosystem Restoration Projects. *Ecol. Eng.* **2000**, *15*, 365–372. [CrossRef]
88. Agüera-Vega, F.; Carvajal-Ramírez, F.; Martínez-Carricondo, P. Assessment of photogrammetric mapping accuracy based on variation ground control points number using unmanned aerial vehicle. *Measurement* **2017**, *98*, 221–227. [CrossRef]
89. Goldstein, E.B.; Oliver, A.R.; de Vries, E.; Moore, L.J.; Jass, T. Ground control point requirements for structure-from-motion derived topography in low-slope coastal environments. *PeerJ PrePrints* **2015**, *3*, e1444v1.
90. Propeller (n.d.). ACCURACY, RELIABILITY, AND SIMPLICITY Using AeroPoints for Aerial Surveying. Available online: https://rtkgpssurveyequipment.com/wp-content/uploads/2019/07/Seco-Propellor-AeroPoints.pdf (accessed on 4 December 2024).

Disclaimer/Publisher's Note: The statements, opinions and data contained in all publications are solely those of the individual author(s) and contributor(s) and not of MDPI and/or the editor(s). MDPI and/or the editor(s) disclaim responsibility for any injury to people or property resulting from any ideas, methods, instructions or products referred to in the content.